INTERNATIONAL JOURNAL FOR NUMERICAL METHODS IN FLUIDS
Int. J. Numer. Meth. Fluids 2004; **46**:569–606 (DOI: 10.1002/fld.760)

Godunov-type adaptive grid model of wave–current interaction at cuspate beaches

Benedict D. Rogers, Alistair G. L. Borthwick* and Paul H. Taylor

Department of Engineering Science, University of Oxford, Parks Road, Oxford, OX1 3PJ, U.K.

SUMMARY

This paper presents a second-order accurate Godunov-type numerical scheme for depth- and period-averaged wave–current interaction. A flux Jacobian is derived for the wave conservation equations and its eigensystem determined, enabling Roe's approximate Riemann solver to be used to evaluate convective fluxes. Dynamically adaptive quadtree grids are used to focus on local hydrodynamic features, where sharp gradients occur in the flow variables. Adaptation criteria based on depth-averaged vorticity, wave-height gradient, wave steepness and the magnitude of velocity gradients are found to produce accurate solutions for nearshore circulation at a half-sinusoidal beach. However, the simultaneous combination of two or more separate criteria produces numerical instability and interference unless all criteria are satisfied for mesh depletion. Simulations of wave–current interaction at a multi-cusped beach match laboratory data from the United Kingdom Coastal Research Facility (UKCRF). A parameter study demonstrates the sensitivity of nearshore flow patterns to changes in relative cusp height, angle of wave incidence, bed roughness, offshore wave height and assumed turbulent eddy viscosity. Only a small deviation from normal wave incidence is required to initiate a meandering longshore current. Nearshore circulation patterns are highly dependent on the offshore wave height. Reduction of the assumed eddy viscosity parameter causes the primary circulation cells for normally incident waves to increase in strength whilst producing rip-like currents cutting diagonally across the surf zone. Copyright © 2004 John Wiley & Sons, Ltd.

KEY WORDS: wave–current interaction; Godunov; grid adaptation; cuspate beaches

1. INTRODUCTION

Numerical models are commonly used to predict coastal processes, including hydrodynamics, sediment transport and the evolution of bed morphology. Localized relatively small-scale flow features such as shear layers can have profound effects on fluid mixing and material transport, so fine resolution modelling is essential. The simulation of localized flow features on fixed

---

*Correspondence to: A. G. L. Borthwick, Department of Engineering Science, University of Oxford, Parks Road, Oxford, OX1 3PJ, U.K.

Contract/grant sponsor: U.K. Engineering and Physical Sciences Research Council; contract/grant number: EPSRC Grant GR/L29877

Received 5 May 2003
Revised 16 April 2004

regular grids of uniformly fine resolution is computationally inefficient. Dynamic grid refinement overcomes this problem, and is well established in many areas of CFD. Techniques that include adaptive unstructured grids [1], adaptive hierarchical grids [2] and block refinement are becoming increasingly popular [3].

The main techniques used to activate grid refinement (which is interchangeably referred to as adaptation herein) involve adapting the mesh according to either a physically based criterion, or according to an approximate error estimate in the solution. When error assessments (or convergence of variable residuals) drive mesh adaptation, *a priori* error estimates commonly use a least-squares approximation to the approximate solution (e.g. References [4–6]). However, such approaches are influenced by the error in the approximate solution as opposed to following physical flow features (as recommended by George [7]).

Shallow flow modellers make use of the two-dimensional shallow water equations (SWEs) which describe the hydrodynamics in water bodies where the horizontal dimensions of motion are far greater than the depth. Incorporation of grid adaptation in a numerical solver of the SWEs facilitates modelling the evolution of locally fine-scaled flow behaviour. Amongst others, Ivanenko and Muratova [8] used optimization of a harmonic-functional to adjust the shape of a curvilinear grid when using the SWEs to model flow in the Azov Sea. Borthwick *et al.* [9] obtained satisfactory results for the SWEs against standard benchmark test cases when using adaptive quadtree grids with individual cell circulation as the adaptivity criterion. Similarly, Rogers *et al.* [10] used criteria based on non-dimensionalized depth-averaged vorticity and the magnitude of the free-surface gradient to resolve flows in a circular reservoir, two-dimensional dam-breaks and oblique hydraulic jumps. Sleigh *et al.* [5] used an approximate error estimator to adapt triangular unstructured grids for two-dimensional dam-break simulations. For coastal simulations, Borthwick and Park [11] used quadtree grids in a 2-D combined wave and current scheme. The grids were adapted according to either the magnitude of a longshore current or the depth-averaged vorticity, in order to provide one extra level of resolution for nearshore circulation patterns. Hubbard and Dodd [12] used adaptive mesh-block refinement with Cartesian grids to study overtopping of coastal defences by increasing grid resolution as the water shallowed.

Although it is well established that grid adaptation is an efficient approach to model shallow water flow features of various scales and locations [3], little attention has been given to evaluating the effectiveness of different criteria, their combination, and how frequently adaptation should occur in shallow coastal flow simulations. Hence, this paper examines different adaptation criteria based on local flow variables using dynamically adaptive quadtree grids within a numerical scheme for shallow water and coastal hydrodynamics. Quadtree grids are easy to adapt due to their hierarchical ordered data-tree structure, refinement merely involving addition or subtraction of leaf cells with little computational overhead.

Numerical modelling of highly sheared localized coastal flows, such as occur near the edges of regions with strong currents, demands appropriate discretization schemes. Shallow water flows that exhibit large gradients in the flow variables or local discontinuities (referred to as Riemann problems) can now be modelled with great accuracy using high-resolution Godunov-type methods e.g. References [13, 14]. Hubbard and Dodd [12] have recently applied a Godunov-type solver to the SWEs for coastal hydrodynamics.

This paper describes the application of high-resolution Godunov-type methods and dynamically adaptive quadtree grids to combined wave–current flows. The governing equations for 2-DH depth- and period-averaged combined wave and current flow are given in Section 2.

These are discretized using finite volumes to develop a second-order accurate Godunov-type numerical scheme. A flux Jacobian and its associated eigensystem are derived for the wave energy and kinematic wave number conservation laws. Section 3 describes the quadtree grid generation methodology. Section 4 presents a detailed study of different adaptation criteria for wave-induced currents at a half-sinusoidal beach. Simulations of normally and obliquely incident waves propagating towards a tri-cuspate beach are discussed in Section 5. The numerical model is used to investigate the sensitivity of nearshore wave-induced currents to changes in incident wave height and angle, bed roughness, relative cusp height and assumed turbulent eddy viscosity.

2. NUMERICAL SOLUTION

2.1. Theoretical background of the wave–current model

A period-averaged formulation for a ray-type wave–current interaction model is used here to model relatively large coastal areas. The wave motion is assumed to be gravity-driven and irrotational, vertical motions are negligible so that pressure is hydrostatic, and small amplitude waves propagate over a mild-slope with negligible non-linear wave–wave interaction.

2.2. Governing equations of wave–current interaction

By considering the number of free-surface wave crests per unit length crossing a position (x, y) per unit time and the absolute frequency, σ, of waves relative to a fixed bed, the conservation of waves is expressed by [15]

$$\frac{\partial \mathbf{K}}{\partial t} + \nabla\sigma = \mathbf{0} \tag{1}$$

where the wave number vector, $\mathbf{K}$, can be considered to be the density of the waves and σ, the flux of waves. The wave number or wave direction vector, $\mathbf{K}$, is expressed in terms of its co-ordinate components $K_x = K\cos\theta$, and $K_y = K\sin\theta$ such that

$$K = |\mathbf{K}| = \sqrt{K_x^2 + K_y^2} \tag{2}$$

For a mass of water moving at velocity $\mathbf{U}$, the absolute frequency of the waves, σ, is related to the frequency of the waves relative to the moving mass of water, σ_0, by the Doppler relation

$$\sigma = \sigma_0 + \mathbf{K}\cdot\mathbf{U} \tag{3}$$

Furthermore, a modified linear dispersion relation holds for waves propagating up a sloping beach [16], which for mild slopes reduces to the familiar linear dispersion relation

$$\sigma_0^2 = kg\tanh kh \tag{4}$$

where k is the separation factor, h is the local water depth, and g is the acceleration due to gravity. As shown by Battjes [17], the wave number K and the separation factor k are related by

$$K^2 = k^2 + \delta^* = k^2(1+\delta) \tag{5}$$

where the diffraction term $\delta^* = (\nabla^2 a)/a$ is amplitude curvature. Inclusion of δ^* allows the ray-type approach to include the effects of diffraction, such as in caustic zones [18]. Herein, the numerical model is not applied to cases involving strong diffraction which would be better modelled by a mild-slope or Boussinesq solver, so $\delta^* \approx 0$.

By substituting the dispersion relation (4) and the Doppler relation (3) into the wave conservation equation (1) and utilizing the Battjes relation (5), Yoo [16] (in detail) and also Yoo and O'Connor [18] derived depth- and period-averaged equations describing conservation of mass, momentum, wave energy density and kinematic wave number. Herein, the resulting governing equations that describe conservation of mass and momentum will referred to as modified shallow water equations (SWEs), and those that describe conservation of wave energy density and kinematic wave number will be denoted as wave conservation equations (WCEs) — see also Section 2.3. Thus, we write the equations expressing wave–current interaction in integral form as

$$\frac{\partial}{\partial t}\int_\Omega \mathbf{q}\,\mathrm{d}\Omega + \int_\Omega \left(\frac{\partial \mathbf{f}}{\partial x} + \frac{\partial \mathbf{g}}{\partial y}\right)\mathrm{d}\Omega = \int_\Omega \mathbf{h}\,\mathrm{d}\Omega \tag{6}$$

where for the modified SWEs, the vectors $\mathbf{q}, \mathbf{f}, \mathbf{g}$ and $\mathbf{h}$ are given by

$$\mathbf{q} = \begin{bmatrix} \eta \\ uh \\ vh \end{bmatrix}, \quad \mathbf{f} = \begin{bmatrix} uh \\ u^2h + \frac{1}{2}(\eta^2 + 2\eta h_s)g - \varepsilon_x h\,\frac{\partial u}{\partial x} \\ uvh - \varepsilon_x h\,\frac{\partial v}{\partial x} \end{bmatrix}, \quad \mathbf{g} = \begin{bmatrix} vh \\ uvh - \varepsilon_y h\,\frac{\partial u}{\partial y} \\ v^2h + \frac{1}{2}(\eta^2 + 2\eta\, h_s)g - \varepsilon_y h\,\frac{\partial v}{\partial y} \end{bmatrix}$$

$$\text{and}\quad \mathbf{h} = \begin{bmatrix} 0 \\ \dfrac{\tau_{wx} - \tau_{bx}}{\rho} + g\eta\,\dfrac{\partial h_s}{\partial x} - \dfrac{1}{\rho}\left(\dfrac{\partial S_{xx}}{\partial x} + \dfrac{\partial S_{xy}}{\partial y}\right) \\ \dfrac{\tau_{wy} - \tau_{by}}{\rho} + g\eta\,\dfrac{\partial h_s}{\partial y} - \dfrac{1}{\rho}\left(\dfrac{\partial S_{yx}}{\partial x} + \dfrac{\partial S_{yy}}{\partial y}\right) \end{bmatrix} \tag{7}$$

while the vectors for the WCEs are written as

$$\mathbf{q} = \begin{bmatrix} E \\ K_x \\ K_y \end{bmatrix}, \quad \mathbf{f} = \mathbf{f}^{\mathrm{W}} + \mathbf{f}^{\mathrm{WCI}} = \begin{bmatrix} EC_{gx} \\ \sigma_0 \\ 0 \end{bmatrix} + \begin{bmatrix} uE \\ uK_x + vK_y \\ 0 \end{bmatrix} = \begin{bmatrix} EC_{gx} + uE \\ \sigma_0 + uK_x + vK_y \\ 0 \end{bmatrix}$$

$$\mathbf{g} = \mathbf{g}^{\mathrm{W}} + \mathbf{g}^{\mathrm{WCI}} = \begin{bmatrix} EC_{gy} \\ 0 \\ \sigma_0 \end{bmatrix} + \begin{bmatrix} vE \\ 0 \\ uK_x + vK_y \end{bmatrix} = \begin{bmatrix} EC_{gy} + vE \\ 0 \\ \sigma_0 + uK_x + vK_y \end{bmatrix}$$

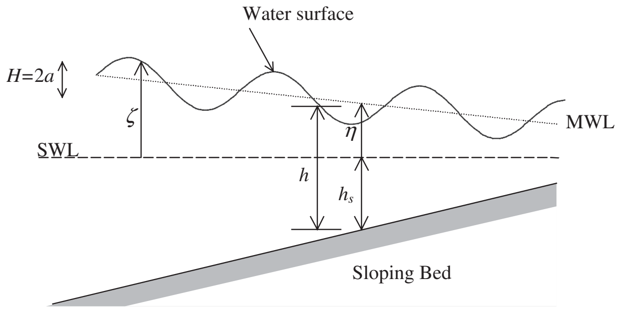

Figure 1. Definition sketch for numerical scheme.

and

$$\mathbf{h}=\begin{bmatrix} -\left(S_{xx}\dfrac{\partial u}{\partial x}+S_{xy}\dfrac{\partial u}{\partial y}+S_{yx}\dfrac{\partial v}{\partial x}+S_{yy}\dfrac{\partial v}{\partial y}\right)-\rho g a C^a a^2+\left(\varepsilon_x\dfrac{\partial^2 a}{\partial x^2}+\varepsilon_y\dfrac{\partial^2 a}{\partial y^2}\right)\dfrac{\rho g a}{2} \\ -C_{gy}\dfrac{\partial K_x}{\partial y}-S_h\dfrac{\partial h_s}{\partial x}+\dfrac{C_g}{2k}\dfrac{\partial \delta^*}{\partial x} \\ -C_{gx}\dfrac{\partial K_y}{\partial x}-S_h\dfrac{\partial h_s}{\partial y}+\dfrac{C_g}{2k}\dfrac{\partial \delta^*}{\partial y} \end{bmatrix} \tag{8}$$

where superscripts W and WCI refer to wave and wave–current interaction fluxes. In these conservation equations (see one-dimensional definition sketch in Figure 1), η is the period-averaged surface elevation (set-up and set-down) above the still water level h_s, h $(=\eta+h_s)$ is the total water depth, u and v are period- and depth-averaged velocity components in the x- and y-directions respectively, ρ is water density, τ_{wx}, τ_{wy} and τ_{bx}, τ_{by} are surface and bed friction stresses, $E=\rho g a^2/2$ is the wave energy per wave per unit crest length, a is the wave amplitude, K_x and K_y are the wave number components in the x- and y-directions, respectively, C_{gx} and C_{gy} are the group celerity components of the total group celerity C_g, k is the separation factor, C^a is a bottom friction coefficient associated with the wave amplitude, S_h is a depth-associated frequency response factor, ε_x and ε_y are the kinematic eddy viscosity coefficients, and S_{xx}, S_{xy}, S_{yx}, S_{yy} are radiation stress tensors representing the excess momentum flux due to waves [19]. In tensor notation, the group celerities are given by

$$C_{gi}=\frac{K_i}{k}C_g=\frac{1}{2}(1+G)\frac{\sigma_0}{k}\frac{K_i}{k}=\frac{1}{2}(1+\delta)(1+G)\frac{\sigma_0}{K}\frac{K_i}{K} \tag{9}$$

where

$$C_g=(1+G)\sigma_0/(2k)=kG^K \quad \text{and} \quad G=\frac{2kh}{\sinh 2kh} \tag{10}$$

The depth-associated frequency response factor S_h is given by

$$S_h=\frac{\partial \sigma_0}{\partial h}=\frac{k\sigma_0}{\sinh 2kh}=\frac{G\sigma_0}{2h} \tag{11}$$

The radiation stress tensor is given by [18,19]

$$S_{ij} = \frac{1}{2}\left[(1+G)\frac{K_i}{k}\frac{K_j}{k} + G\delta_{ij}\right]E \tag{12}$$

where δ_{ij} is the Kronecker delta.

The third-order terms in Equation (8) are a direct result of including the Battjes relation to account for the lateral transfer of wave energy along the wave crest during instances where δ^* is non-zero, (see Reference [16] for a derivation of these terms).

The friction coefficient C^a, wave breaking criterion and kinematic eddy viscosity are estimated empirically using Bijker's [20], US-CERC [21] and Thornton's [22] formulae, respectively. More sophisticated closure submodels could be utilized (see Reference [23]) but are not implemented here, as the purpose of this paper is to evaluate the use of dynamically adaptive grids with a Godunov-type numerical scheme for coastal hydrodynamics. The eddy viscosities, ε_x and ε_y are assumed isotropic and controlled by an empirical factor M_{T}:

$$\varepsilon_x = \varepsilon_y = M_{\mathrm{T}} A_{\mathrm{b}} \tilde{u}_{\max} \tag{13}$$

where, at the bed, $A_{\mathrm{b}} = a/\sinh(kh) = \tilde{u}_{\max} T/2\pi$ is the excursion length of the orbital motion, $\tilde{u}_{\max} = 2\pi a/T\sinh(kh)$ is the maximum wave particle velocity and T is the wave period.

2.3. Numerical discretization

Comparison of the depth- and period-averaged mass and momentum equations (7) with the shallow water equations (SWEs) of Rogers *et al.* [10] reveals that the only mathematical difference between the two formulations is the additional radiation stress gradients. Thus, Equations (7) for the period- and depth-averaged conservation of mass and momentum can be classified as modified SWEs. The solver developed herein for the wave-induced currents, is essentially the same as that of [10], but with the radiation stress gradient terms treated as source terms for convenience.

Solution of the fully coupled wave–current interaction problem is achieved by solving the WCEs and modified SWEs simultaneously. The governing equations are discretized spatially using finite volumes on collocated Cartesian quadtree grids, with Roe's approximate Riemann solver [24] used for the non-linear convective fluxes in a second-order Godunov-type scheme. Time-integration is performed using the second-order Adams–Bashforth technique with a non-linear limiter applied to suppress the generation of unphysical oscillations. Linear refraction, based on Snell's Law see Reference [15], gives initial estimates of the separation factor and wave number components K_x and K_y in each cell.

Using generalized flux gradient and source term balancing [25] Equation (6) may be written as

$$\frac{\partial}{\partial t}\int_{\Omega} \mathbf{q}\,\mathrm{d}\Omega + \oint_S (\hat{\mathbf{f}} - \hat{\mathbf{f}}^{\mathrm{eq}})\,\mathrm{d}S = \int_{\Omega} \mathbf{h}^*\,\mathrm{d}\Omega \tag{14}$$

where $\hat{\mathbf{f}}$ is the vector of flux functions through S given by $\hat{\mathbf{f}} = \mathbf{f}n_x + \mathbf{g}n_y$ in which n_x and n_y are the Cartesian components of $\mathbf{n}$, the unit normal vector to S, eq refers to equilibrium or still-water values, and $\mathbf{h}^* = \mathbf{h} - \mathbf{h}^{\mathrm{eq}}$. The equations are discretized on a collocated grid with E, K_x, K_y, η, uh and vh stored at the centre of each cell. For each cell, Equation (14) can be more conveniently rewritten as

$$\left.\frac{\partial V\mathbf{q}}{\partial t}\right|_i = -\oint_{\partial C_i} (\hat{\mathbf{f}}_i - \hat{\mathbf{f}}_i^{\mathrm{eq}})\,\mathrm{d}S + (\mathbf{h}_i - \mathbf{h}_i^{\mathrm{eq}})V_i = -\oint_{\partial C_i} \hat{\mathbf{f}}_i'\,\mathrm{d}S + V_i\mathbf{h}_i^* \tag{15}$$

where $\mathbf{q}_i$ and $\mathbf{h}_i$ are the cell centre values, and V_i denotes the area of cell i, ∂C_i is the path of integration, which is along all four cell edges where the flux out of each face is assumed constant. The surface integral in Equation (15) can be evaluated in discrete form by using

$$\oint_{\partial C_i} \hat{\mathbf{f}}_i'\,\mathrm{d}s = (\hat{\mathbf{f}}_{\mathrm{E}}' - \hat{\mathbf{f}}_{\mathrm{W}}' + \hat{\mathbf{f}}_{\mathrm{N}}' - \hat{\mathbf{f}}_{\mathrm{S}}')\Delta s \tag{16}$$

where $\hat{\mathbf{f}}_{\mathrm{E}}'$, $\hat{\mathbf{f}}_{\mathrm{W}}'$, $\hat{\mathbf{f}}_{\mathrm{N}}'$ and $\hat{\mathbf{f}}_{\mathrm{S}}'$ are the vector fluxes through the east, west, south and north faces of each cell, and Δs is the length of the side of the cell. At each cell edge, the convective fluxes are evaluated using Roe's approximate Riemann solver [24]:

$$\mathbf{f}_{i,j} = \frac{1}{2}[\mathbf{f}(\mathbf{q}_{i,j}^+) + \mathbf{f}(\mathbf{q}_{i,j}^-) - |\mathbf{A}|(\mathbf{q}_{i,j}^+ - \mathbf{q}_{i,j}^-)] \tag{17}$$

in which

$$|\mathbf{A}| = \mathbf{R}|\Lambda|\mathbf{L} \tag{18}$$

where $\mathbf{q}_{i,j}^+$ and $\mathbf{q}_{i,j}^-$ are the reconstructed right and left Riemann states, respectively, at the cell interface located between adjacent cells i and j, $\mathbf{A}$ is the flux Jacobian evaluated using $\mathbf{R}$ and $\mathbf{L}$ the right and left eigenvector matrices of $\mathbf{A}$, respectively, and $|\Lambda|$ is a diagonal matrix of the absolute values of the eigenvalues of $\mathbf{A}$. The flux Jacobian matrix is given by

$$\begin{aligned}\mathbf{A} &= \frac{\partial \mathbf{f}^{\mathrm{W}}}{\partial \mathbf{q}}\\ &= \begin{bmatrix} C_{gx}n_x + C_{gy}n_y & (K_x \frac{\partial G^K}{\partial K_x} + G^K)En_x + K_y \frac{\partial G^K}{\partial K_x} En_y & K_x \frac{\partial G^K}{\partial K_y} En_x + (K_y \frac{\partial G^K}{\partial K_y} + G^K)En_y \\ 0 & (C_{gx} + S_h \frac{\partial \eta}{\partial K_x})n_x & 0 \\ 0 & 0 & (C_{gy} + S_h \frac{\partial \eta}{\partial K_y})n_y \end{bmatrix}\end{aligned} \tag{19}$$

with

$$G^K = C_g/k \quad \text{and} \quad \frac{\partial G^K}{\partial K_i} = \frac{\partial G^K}{\partial k}\frac{\partial k}{\partial K_i} = \left(\frac{\sigma_0}{k^3}\left[\frac{kh}{\tanh kh} - \frac{2kh}{\tanh 2kh} - \frac{3}{2}\right] + \frac{C_g^2}{\sigma_0 k}\right)\frac{\partial k}{\partial K_i}$$

The matrix $\mathbf{A}$ has eigenvalues given by

$$\lambda_1 = C_{gx}n_x + C_{gy}n_y, \quad \lambda_2 = C_{gx}n_x + S_h\frac{\partial \eta}{\partial K_x}n_x, \quad \lambda_3 = C_{gy}n_y + S_h\frac{\partial \eta}{\partial K_y}n_y \tag{20}$$

These real and distinct eigenvalues denote the characteristic velocities of propagation of the energy flux and the wave number, and confirm that the scheme for the wave fluxes is strictly hyperbolic. The eigenvalues λ_2 and λ_3 show that the propagation velocity is modified by the depth-associated frequency response factor S_h as the wave number components advance over varying depth water. The associated right and left eigenvector matrices are

$$\mathbf{R}=\begin{bmatrix} 1 & A_{12} & A_{13} \\ 0 & S_h \dfrac{\partial \eta}{\partial K_x} n_x & 0 \\ 0 & 0 & S_h \dfrac{\partial \eta}{\partial K_y} n_y \end{bmatrix}$$

$$\text{and} \quad \mathbf{L}=\begin{bmatrix} 1 & -A_{12}\left(S_h \dfrac{\partial \eta}{\partial K_x} n_x\right)^{-1} & -A_{13}\left(S_h \dfrac{\partial \eta}{\partial K_y} n_y\right)^{-1} \\ 0 & \left(S_h \dfrac{\partial \eta}{\partial K_x} n_x\right)^{-1} & 0 \\ 0 & 0 & \left(S_h \dfrac{\partial \eta}{\partial K_y} n_y\right)^{-1} \end{bmatrix} \tag{21}$$

where A_{12} and A_{13} are elements of the flux Jacobian given in Equation (19).

Thus, in summary, at the beginning of each time step the conserved variables, $\mathbf{q}$, are stored at the cell centres in a collocated (i.e. non-staggered) form, these are interpolated to the cell face (or Riemann state) values in a physical manner using the slope limiter (see next subsection and Equations (22) to (24) which are then used to calculate the intercell fluxes of Equation (17)).

Slope limiter. The variables E, K_x and K_y in Equations (19)–(21) are given by Roe's average state, which is defined as

$$E=\sqrt{E^{+}E^{-}}, \quad K_x=\frac{K_x^{+}\sqrt{E^{+}}+K_x^{-}\sqrt{E^{-}}}{\sqrt{E^{+}}+\sqrt{E^{-}}} \quad \text{and} \quad K_y=\frac{K_y^{+}\sqrt{E^{+}}+K_y^{-}\sqrt{E^{-}}}{\sqrt{E^{+}}+\sqrt{E^{-}}} \tag{22}$$

where the superscripts + and − denote the right and left Riemann states either side of a cell interface respectively. A MUSCL-type slope limiter is also used for piecewise-linear variable reconstruction within the cell to estimate the values of the Riemann states and render the scheme second-order accurate in space see Reference [26]. At each time step, the reconstruction step is carried out independently for each spatial direction. This limiter is implemented such that for consecutive cells $i-1, i, i+1$ in a co-ordinate direction on a locally uniform grid (using interpolation if necessary):

$$q_{i\pm\frac{1}{2}}=q_i \pm \tfrac{1}{2}(q_i-q_{i-1})\Phi(r) \tag{23}$$

where $\Phi(r)$ is defined by

$$\Phi(r)=\max[0, \min(\beta r, 1), \min(r, \beta)] \tag{24}$$

with $1 \leqslant \beta \leqslant 2$ and $r=(q_{i+1}-q_i)/(q_i-q_{i-1})$. Additionally, the entropy fix of Harten and Hyman [27] is used to avoid the numerical solution violating entropy considerations. Equation (15) is then integrated in time using a second-order Adams–Bashforth scheme.

Wave–current interaction fluxes and source terms. Roe's approximate Riemann solver is used to evaluate the wave fluxes, $\mathbf{f}^{W}$, given by Equation (8), because it is extremely difficult to derive a flux Jacobian with an associated eigensystem that incorporates currents as well as waves. The wave–current interaction fluxes, $\mathbf{f}^{WCI}$, can be evaluated at the centre of each cell face by using values that ensure the inherent conservation form of the finite volume scheme. This is most readily achieved using Roe-type averages, already defined at the required locations by equations such as (22).

The source vector **h** contains spatial gradients that cannot be expressed easily in flux gradient form. In all cases, these have been calculated using central difference approximations interpolated to a uniform surrounding grid if necessary (see Section 3). For the non-diffractive results presented herein the gradients of the diffraction term δ^* are all set to zero.

Boundary conditions. The inflow and outflow boundary conditions for currents are as given by Reference [10]. For the period-averaged wave equations, non-reflective transmissive boundary conditions are applied at offshore, onshore and lateral boundaries to allow transient waves to leave the domain:

$$\phi_{\mathrm{B}} = \phi_{\mathrm{I}}, \tag{25}$$

where $\phi = K_x, K_y, E$. Subscript B denotes the boundary value, and subscript I denotes the inner Riemann state value at the boundary. The value of ϕ_{B} is only pre-specified at the offshore boundary according to the prescribed conditions. To account for the moving shoreline, the wetting and drying scheme of Reference [28] is used.

3. QUADTREE GRID GENERATION AND ADAPTATION

The quadtree grid generator and data handling techniques are described in detail by Reference [10]. In short, the method involves domain decomposition into square or rectangular tiles according to prescribed geometric/flow criteria. Cell numbering and neighbour finding by means of the nearest neighbour concept rely on the quadtree structure see e.g. Reference [29]. The physical variables are stored in a collocated arrangement on the grid.

Grid adaptation is undertaken at fixed intervals during the flow simulation, the interval being a multiple of the time step used in integrating the governing equations. Adaptation is carried out according to prescribed hydrodynamic criteria, which are compared against the values of given hydrodynamic parameters evaluated numerically at each cell in the grid. Where gradients of the hydrodynamic dependent variables are used as adaptation parameters, these are calculated using central differences interpolated to a surrounding uniform grid of equivalent resolution if necessary.

Grid enrichment is achieved by cell subdivision, if the hydrodynamic parameter calculated for the cell exceeds the maximum prescribed value. Grid coarsening involves cell removal as follows. If all four cells with the same parent cell have values of the hydrodynamic parameter that are less than the prescribed minimum value, then all four cells are removed. Once mesh refinement is complete, grid regularization is enforced ensuring that the maximum linear ratio between any adjacent cells remains 2:1. It should be noted that the resolution levels used throughout adaptive simulations are user-defined maximum and minimum subdivision levels. Addition and removal of cells then creates the problem of assigning values to cell variables to allow the flow simulation to continue such that it does not violate mass and momentum conservation. We use the prolongation routines and restriction routines of Reference [30] whereby new cell data are linearly interpolated from surrounding cells.

Within the numerical scheme, the wetting and drying scheme is used simultaneously with grid adaptation at the shoreline. In order to ensure that these two processes do not interfere, at the end of each time step wetting is performed first in the x-direction, and then in the y-direction (and then similarly for drying). Only when wetting and drying of the shoreline is complete does adaptation take place.

4. SIMULATION OF NEARSHORE CIRCULATION AT A HALF-SINUSOIDAL BEACH

4.1. *Nearshore circulation at a sinusoidal beach*

Most real beaches have non-planar bathymetries and consequently, there exist alongshore variations of the wave field. Currents are generated by the non-uniformity of wave heights due to topographical or wind forcing variations; these currents appear as patterns of longshore currents, rip currents and circulation cells. In addition to the variation of the mean water level (MWL), these nearshore currents help balance the driving forces.

Experimental data on near shore circulation at a laboratory-scale sinusoidal beach obtained by da Silva Lima [31] are used to verify the numerical scheme and thence to assess grid adaptation criteria. The half-sinusoidal plywood beach had a still water depth profile $h_s(x, y)$ given by

$$h_{\mathrm{s}}(x,y)=\begin{cases} xs & -0.7\,\mathrm{m}\leqslant x\leqslant 0 \\ \left[x-0.75\sin\left(\dfrac{\pi x}{4.36}\right)\sin\left(\dfrac{2\pi y}{\lambda}\right)\right]s & 0\leqslant x\leqslant 4.36\,\mathrm{m} \end{cases} \tag{26}$$

where x is the distance offshore from the still water line (SWL), y is the distance alongshore ranging from 1.5 to 4.5 m, $s = 0.05$ is the slope of the plane beach, and $\lambda = 6$ m, which is referred to as the rip current spacing. Figure 2 shows a plan view of the half-sinusoidal beach in the wave basin.

In the numerical model, a time step of $\Delta t = 0.005$ s is used, and the dimensionless eddy viscosity coefficient M_{T} is set to a value of 1.0 throughout the simulation. For bottom friction, the roughness height is set to 0.001m. The minimum water depth is limited to $D_{\min} = 0.001$m to avoid unrealistically high wave numbers at the shoreline. The incident wave height is ramped up over a period of 20 s. The offshore wave conditions are: wave height $H_{\mathrm{o}} = 0.0618$ m, wave period $T = 0.76$ s, and incident wave angle $\theta_{\mathrm{o}} = 0°$.

4.2. *Grid convergence*

First, grid convergence of the solution is undertaken on uniform quadtree grids of levels 5, 6 and 7. Figure 3 shows the 32×16 uniform quadtree grid where $\Delta x = \Delta y = 0.1875$ m requiring 5 subdivisions of the unit square (referred to as a level-5 grid herein). For the level-6 and level-7 grids, the finest linear cell dimensions are $\Delta x = \Delta y = 0.09375$ m and $\Delta x = \Delta y = 0.046875$ m, respectively. Grid convergence is assessed using Roache's [32] grid

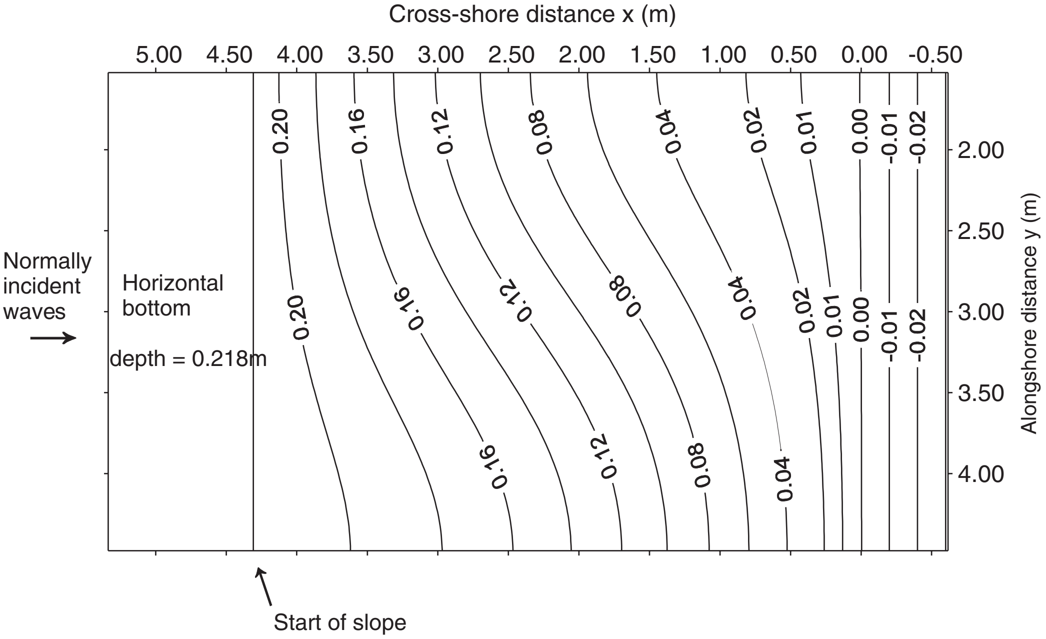

Figure 2. Sinusoidal beach: definition sketch.

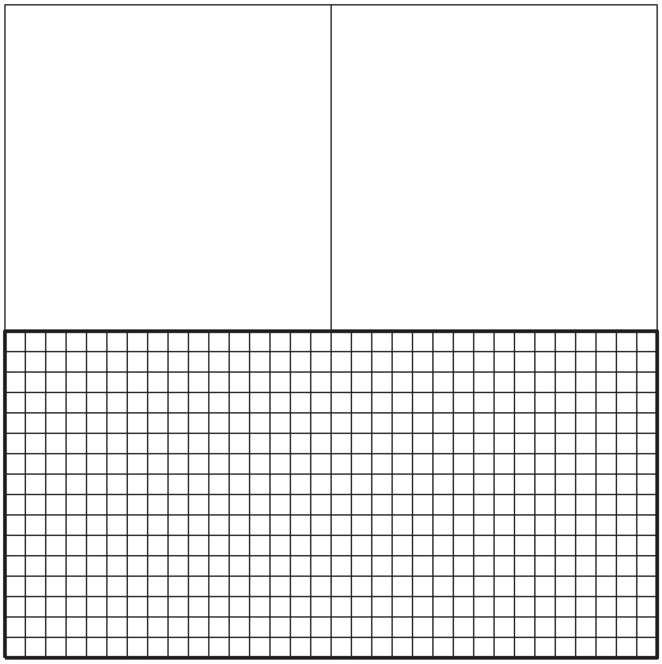

Figure 3. Level-5 uniform quadtree grid ($\Delta x = \Delta y = 0.1875\,\mathrm{m}$).

convergence index (GCI). Using the L_2 norm of the velocity (see Reference [4]), the GCI is 22% from the level-5 to the level-6 grids, and the GCI is 2% from the level-6 to the level-7 grids. Thus, second-order asymptotic convergence is achieved on the level-7 grid of 8192 cells. Accordingly, treating the converged level-7 result as the true solution, the level-5 depth-averaged velocities have a root mean square error (r.m.s. error) of 4.1% while the level-6 solution has an r.m.s. error of 1.9%. Figure 4 shows da Silva Lima's [31] experimental velocity vectors, and plots of the predicted depth-averaged velocities and stream-function contours obtained using the level-7 grid (the velocities in Figure 4(b) are filtered to an equivalent coarse level-5 grid for ease of visualization). The depth-averaged streamlines delineate a clockwise-rotating primary circulation cell with two counter-clockwise secondary circulation cells, one further up the beach and the other towards the offshore wave-driving boundary. The position of the centre of the computed large primary gyre is displaced alongshore relative to the basin centreline, and is 1.74 m from the SWL in close agreement with the experimental result of da Silva Lima where the gyre is approximately 1.7 m from the SWL. Our second-order finite-volume scheme predicts more accurately the location of the centre of the gyre than Borthwick and Park's [11] first-order finite difference scheme.

Predicted wave heights along the cross-shore basin-centreline displayed in Figure 5 are in close agreement with the results of Reference [11] and the experimental data of da Silva Lima. Despite the absence of non-linear shoaling and non-linear decay of the broken wave heights in the numerical scheme, the results indicate that the wave-breaking criterion is well suited to this application.

Figure 6 shows contour plots of wave crests when a crest is at the offshore wave-driving boundary. The wave phase is predominantly affected by the bottom topography, and little affected by the recirculating currents. Only after the waves have broken inside the surf zone where the physical meaning of the wave number is unclear, are there rapid changes in wave phase. The offshore-flowing current has a slight influence on the phase of the incoming waves because the wave model is based on linear potential theory with a linear dispersion relation.

4.3. *Grid adaptation criteria*

With a converged solution available, the performance of the following five adaptation criteria is investigated:

- Criterion I: non-dimensionalized depth-averaged vorticity;
- Criterion II: non-dimensionalized r.m.s. velocity gradient magnitude;
- Criterion III: wave steepness;
- Criterion IV: magnitude of wave height gradient; and
- Criterion V: wave height gradient non-dimensionalized with respect to cell size.

The level-5 32×16 grid of Figure 3 is used as the base grid for adaptation. A user-defined maximum cell size is restricted to level 5, and the minimum cell size is restricted to that of grid convergence, level 7. Dynamic grid adaptation takes place every time step.

Criterion I: The grid is adapted according to the value of the absolute depth-averaged vorticity non-dimensionalized with respect to the wave period T:

$$\Omega_0 = T \left| \frac{\partial u}{\partial y} - \frac{\partial v}{\partial x} \right| \tag{27}$$

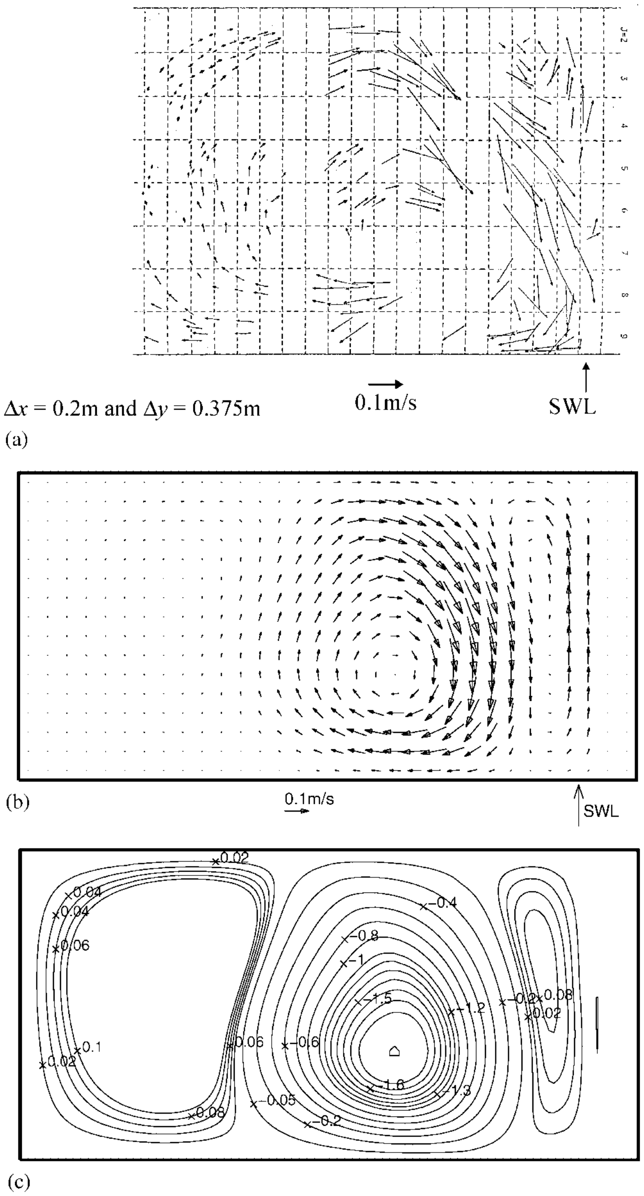

Figure 4. Comparison of converged level-7 ($\Delta x = \Delta y = 0.046875$ m) prediction with experimental data for flow over a half-sinusoidal beach [31]: (a) Experimental velocity vectors [31]; (b) filtered depth-averaged velocities (equivalent to $\Delta x = \Delta y = 0.1875$ m); and (c) depth-averaged stream-function contours.

Mesh enrichment takes place if $\Omega_0 > 0.0606$, and mesh depletion if $\Omega_0 < 0.0578$. Figure 7 shows the steady-state adapted quadtree grid, depth-averaged velocity vectors and stream function contours. The major flow features of interest are reproduced properly with an r.m.s. error

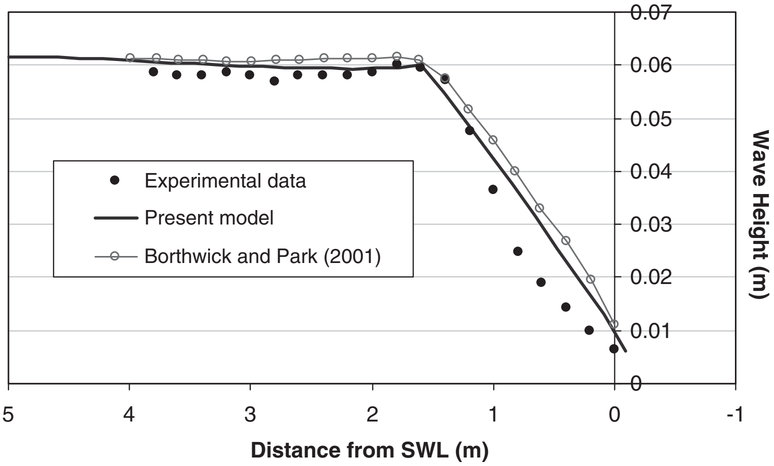

Figure 5. Experimental and predicted wave heights along centreline of basin.

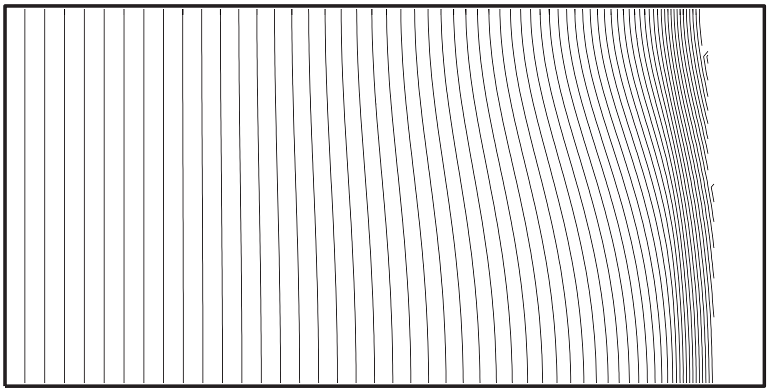

Figure 6. Wave phase contours (also crest lines).

in the velocities of 0.65% when compared with the accurate solution of the uniform level-7 case. The nature of the weaker offshore circulation cell has changed due to the lack of grid resolution in this area, but this gyre is far weaker than the nearshore primary and secondary ones. The adapted grid has 3359 cells, with high cell density in the vicinity of the two main flow circulation zones. As also found by Reference [10] for jet-forced flow in a circular reservoir, an adaptivity criterion based on depth-averaged vorticity gives accurate results efficiently.

Criterion II: The grid is adapted according to the non-dimensionalized r.m.s spatial velocity gradient magnitude:

$$V_s = T\sqrt{\left(\frac{\partial u}{\partial x}\right)^2 + \left(\frac{\partial u}{\partial y}\right)^2 + \left(\frac{\partial v}{\partial x}\right)^2 + \left(\frac{\partial v}{\partial y}\right)^2} \tag{28}$$

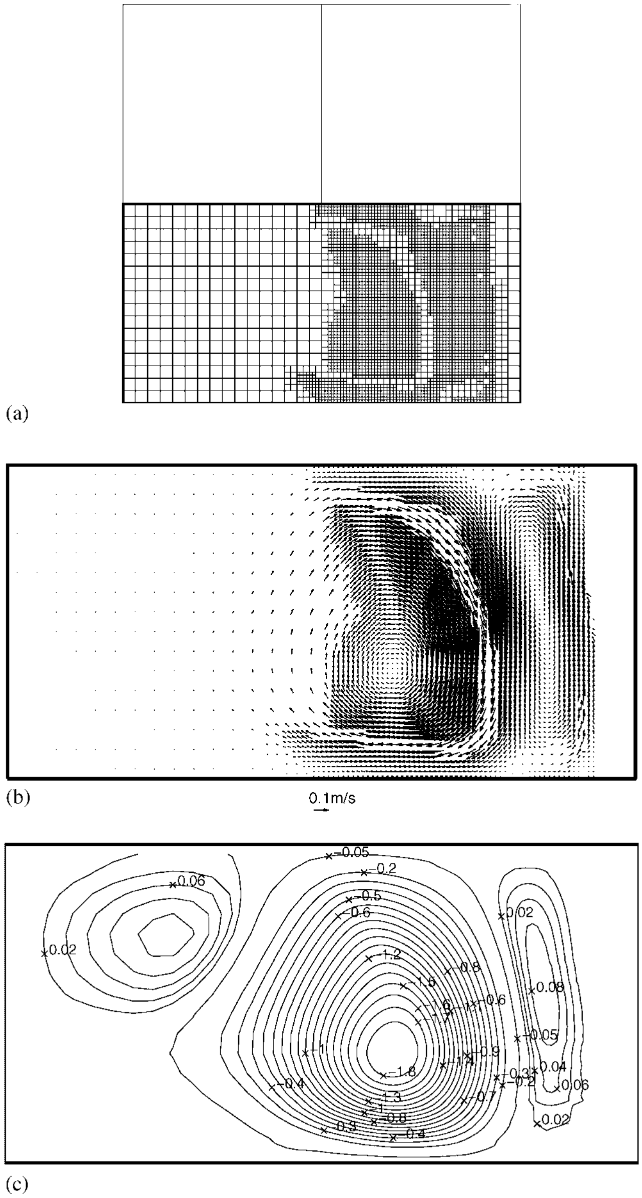

Figure 7. Adaptation based on depth-averaged vorticity: velocity r.m.s. error: 0.65%: (a) Adapted quadtree grid; (b) depth-averaged velocity vectors; and (c) depth-averaged stream-function contours.

Mesh enrichment or depletion is implemented for $V_s > 0.0606$ or $V_s < 0.0578$, respectively. Figure 8(a) illustrates the adapted grid of 3647 cells, which has high cell density in the circulation zones. The flow patterns in Figures 8(a) and 8(b) are accurately modelled, with the velocity r.m.s. error being 0.60%. The main advantage of Criterion II over Criterion I

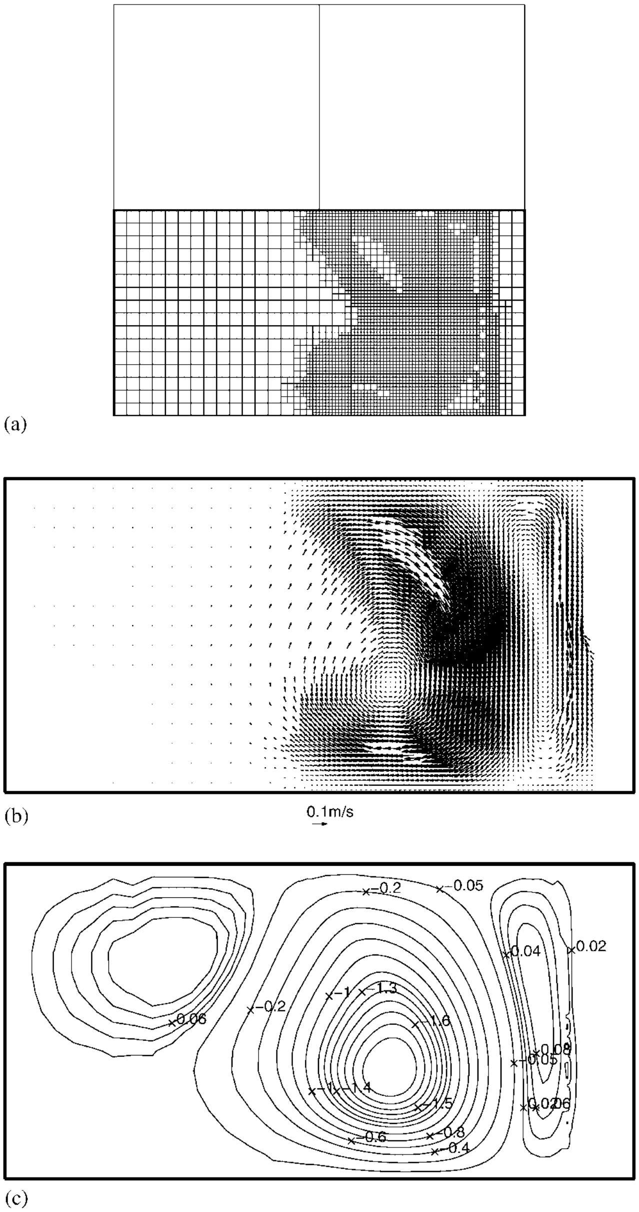

Figure 8. Adaptation based on velocity gradients: velocity r.m.s. error: 0.60%: (a) Adapted quadtree grid; (b) depth-averaged velocity vectors; and (c) depth-averaged stream-function contours.

is that all sharp gradients in the currents are captured in Equation (28), not just the gradients associated with areas of high vorticity. This is evident by comparing Figures 7(a) and 8(a).

Criterion III: The relative wave steepness parameter is defined as

$$R_{\mathrm{w}} = \frac{KH}{K_{\mathrm{o}} H_{\mathrm{o}}} \tag{29}$$

where the subscript o refers to offshore values. In this case, mesh enrichment occurs if $R_w > 1.184$ and mesh depletion if $R_w < 1.125$. With the adapted grid of 2687 cells, the depth-averaged velocity field and stream-function contours in Figure 9 confirm that the flow features are again sensibly predicted. The relative wave steepness parameter creates additional cells either side of the breaker line. There are fewer cells at the shoreline, and the lower resolution leads to slightly larger predicted velocities and a velocity r.m.s. error of 0.89%. The wave steepness criterion is a viable option for grid adaptation, but problems arise in shoreline resolution.

Criterion IV: The magnitude of the wave-height gradient parameter is defined as

$$\left.\frac{\partial H}{\partial x}\right|_i = \sqrt{\left(\frac{\partial H}{\partial x}\right)^2 + \left(\frac{\partial H}{\partial y}\right)^2} \tag{30}$$

for cell i. Mesh enrichment is implemented when $\partial H/\partial x|_i > 0.03$ and depletion if $\partial H/\partial x|_i < 0.0285$. Figure 10(a) shows the adapted grid of 2318 cells. Criterion IV produces additional cells almost solely in the surf zone immediately after wave breaking. Cells are also produced in the area immediately adjacent to the shoreline as the wave height rapidly decreases to zero. Figures 10(b) and 10(c) show the associated depth-averaged velocity field and stream function contours respectively. Criterion IV reproduces the main flow features with fewer cells than Criteria I and II, and so is appropriate for generating a locally fine mesh in the surf zone. In this case, the r.m.s. error in velocities is 0.86%.

Criterion V: In order to remove the effect of the grid size on the discretization of gradients, the grid is adapted using an adjusted version of Criterion IV, expressed as

$$\Psi = \sqrt{\left(\frac{\partial H}{\partial x}\right)^2 + \left(\frac{\partial H}{\partial y}\right)^2} \frac{\Delta l}{H_{\mathrm{o}}} \tag{31}$$

where Δl is the length of the cell perimeter. Mesh enrichment is enabled if $\Psi > 0.09$, and mesh coarsening occurs if $\Psi < 0.086$. Criterion V leads to unstable results, with many spurious circulation cells generated near the shoreline. This lends support to the idea that adaptation criteria should be based solely on either numerical or physical grounds and not on a combination.

4.4. Combinations of grid adaptation criteria

The question now arises as to what happens if several adaptation criteria that individually produce locally refined grids in specific areas are activated simultaneously. From the foregoing, it appears that Criteria I, II, III and IV are viable control options for grid adaptation.

Combined implementation of Criteria II, III and IV causes the solution to degenerate into many spurious circulation zones. Figure 11 presents the predicted wave-induced current field at $t = 50$ s obtained by jointly applying Criteria II and III. The main nearshore flow features are obtained, but the scheme is unstable due to numerical interference between the different adaptation criteria. Cells that are added after a particular time step due to one criterion may

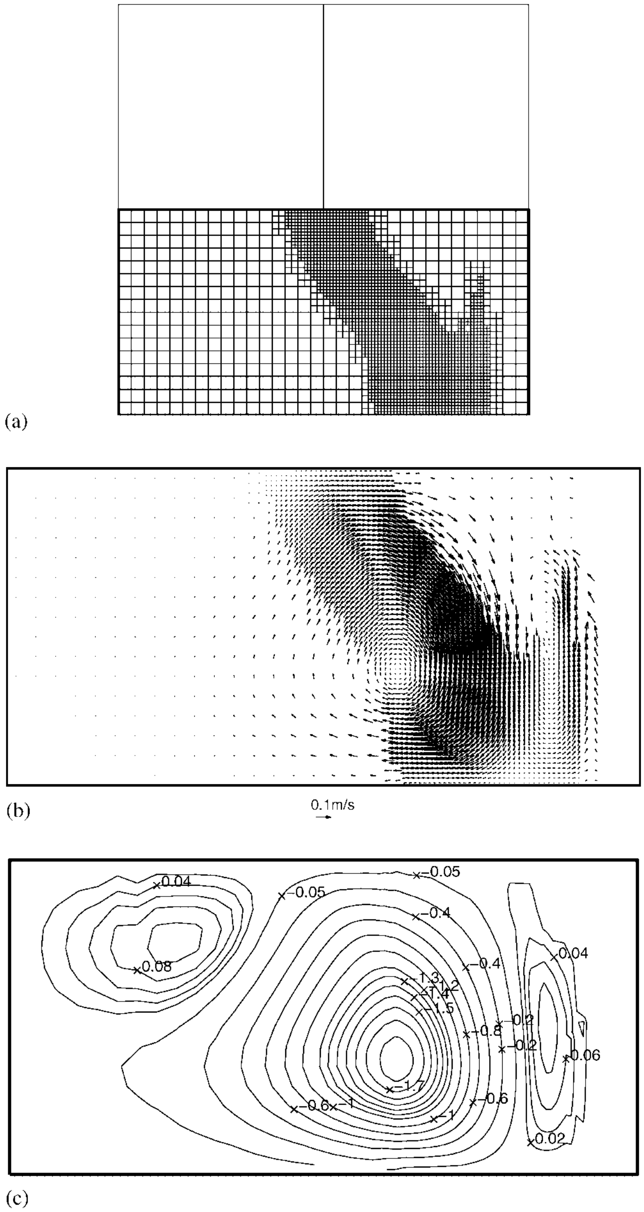

Figure 9. Adaptation based on relative wave steepness: velocity r.m.s. error: 0.89%: (a) Adapted quadtree grid; (b) depth-averaged velocity vectors; and (c) depth-averaged stream-function contours.

be removed by another criterion the next time step causing a feedback mechanism leading to an unstable simulation. Delaying the start of grid adaptation until time $t = 30$ s, and thus allowing the solution to evolve partly, a stable but unsteady scheme is achieved, where the

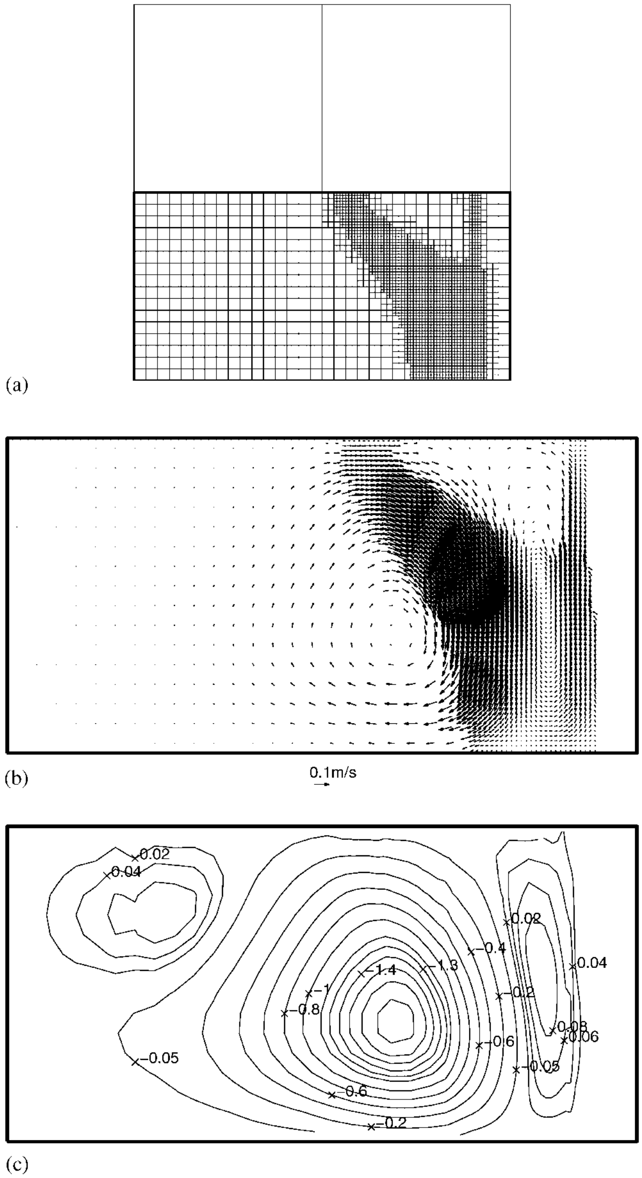

Figure 10. Adaptation based on wave height gradient: velocity r.m.s. error: 0.86%: (a) Adapted quadtree grid; (b) depth-averaged velocity vectors; and (c) depth-averaged stream-function contours.

number of cells in the adapted grid continually fluctuates. Performing the same simulation but allowing the grid to adapt every 100 time steps does not eradicate the non-convergence of the solution with unphysical circulation cells generated in the shallowest waters.

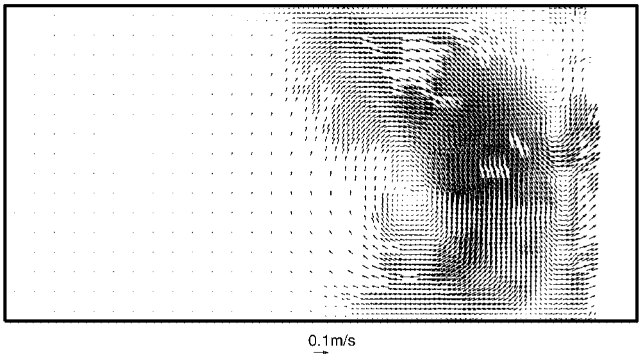

Figure 11. Adaptation based on velocity gradients and wave height gradient: depth-averaged velocity vectors (*unstable*).

If grid adaptation is restricted solely to mesh enrichment, the instability caused by the interference of cell addition and removal according to the separate criteria obviously could not occur. With this in mind, mesh depletion was allowed to occur only when Criteria II and III were satisfied. Figure 12 shows the steady-state adapted quadtree grid, depth-averaged velocities and stream function contours. The simulation is stable, and the grid contains all the extra cells associated with each criterion resulting in an r.m.s. error of 0.53%. This result implies that it is possible to combine criteria only when they all satisfied simultaneously, but at the cost of more cells than were necessary to achieve a reasonably accurate solution.

4.5. *Efficiency of grid adaptation*

The results in Section 4.3 indicate that it is possible to achieve a large reduction in the number of cells while still producing results of almost the same accuracy as obtained on a uniform level 7 grid. This prompts the following questions. Could the same steady-state result be obtained by adapting the grid only every 100, 200, etc. time steps? What are the potential savings in cpu-time? To this end, adaptation is implemented every 1, 2, 4, 8, 16, 64, 128, 256, 512, 1024 and 2048 time steps using Criterion II. The simulation is carried out on a Pentium II 600 MHz single-processor computer with 256 MB RAM. In each case, the solution is run to steady state.

Table I lists the cpu-time for each simulation normalized with respect to the uniformly-dense level-7 solution. It is immediately evident that there is a large saving in cpu-time with a speed-up factor of at least 3, even when using adaptation every time step. There is then a gradual further reduction in cpu-time as larger periods between adaptation are taken. It is only when adaptation is permitted only every 1024 and 2048 time steps that significant reductions in cpu-time are achieved above dynamic adaptation every time step. However, when adaptation is implemented at intervals larger than every 512 time steps, the solution begins to change non-physically, and the investigation is carried no further.

When dynamic adaptation is implemented in the scheme there are slight savings in cpu-time, which indicate that the time taken for adaptation during each iteration step is very small. This is not surprising, given that the grid is not completely regenerated whenever adaptation is invoked. Once the grid reaches near steady state, the grid search to find cells

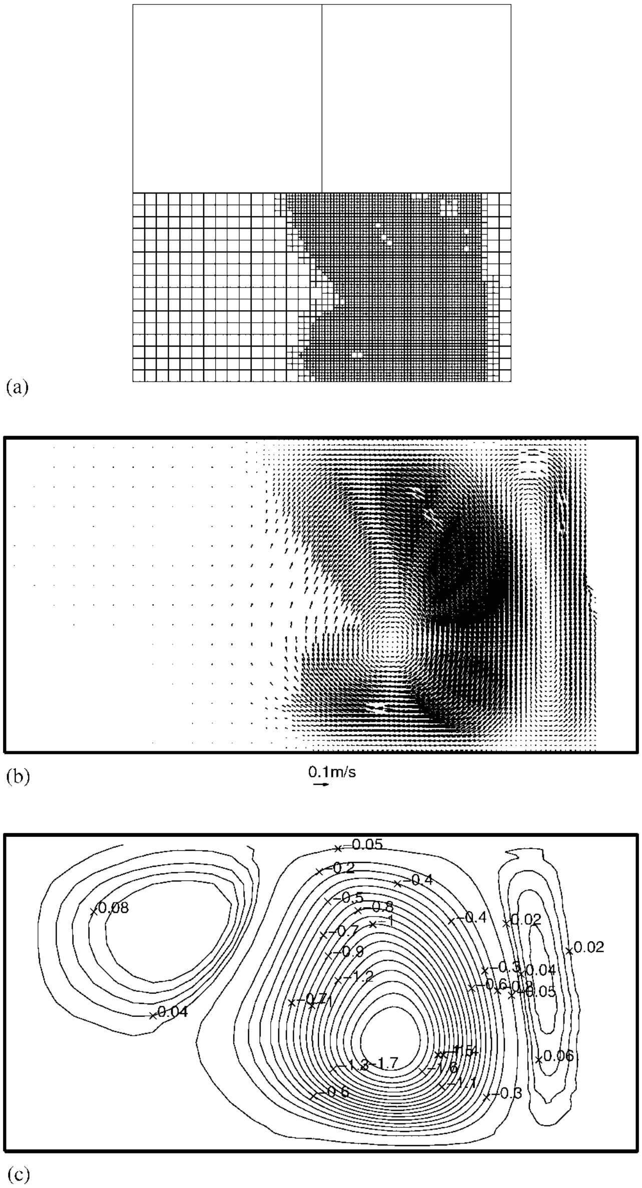

Figure 12. Adaptation based on velocity gradients and wave steepness (both criteria satisfied for mesh depletion): velocity r.m.s. error 0.53%: (a) Adapted quadtree grid; (b) depth-averaged velocity vectors; and (c) depth-averaged stream-function contours.

for removal or addition is very rapid (approximately 2% of the computation time over one time-step). This demonstrates a major advantage of using hierarchical quadtree grids for mesh adaptation.

Table I. Cpu-times for adaptation implemented at different time intervals in comparison with the time for the fully dense grid solution.

Number of time steps between each adaptation of the grid	Cpu-time (s)	Cpu-time normalized with respect to that of the fully dense uniform level-7 grid
1	3122	0.316
2	3055	0.310
4	3023	0.306
8	3014	0.305
16	3004	0.304
64	2995	0.303
128	2980	0.301
256	2950	0.299
512	2896	0.292
1024	2718	0.275†
2048	2402	0.243†
Solution on fully dense uniform level-7 grid	9870	1

†Denotes that solution has changed physically and has not reached steady state by the time the other simulations have finished.
Machine specification: 600 MHz single processor with 256 MB RAM.

The saving in cpu-time, when adaptation occurs every 256 and 512 time steps, arises from the fact that much of the intensive computation during that time is carried out on a coarser grid. This observation is confirmed by Plate 1, which illustrates the growth in cells with time.

In this case, the optimum choice for implementing adaptation lies approximately in the range of every 256–512 time steps. This is not a general result because the optimum choice depends on case-specific parameters (such as offshore wave-period and the maximum allowable time step), and is probably related to the natural time scales of the large scale features of the flow field. Nevertheless, there are minor gains in cpu-time to be achieved by not adapting every time step.

5. WAVE-INDUCED CURRENTS AT A TRI-CUSPATE BEACH IN THE UKCRF

Having identified appropriate grid adaptation criteria for nearshore circulation at a half-sinusoidal beach, the numerical model was applied to wave-induced currents at a fixed tri-cuspate beach in the U.K. Coastal Research Facility (UKCRF) for which measurements have been obtained by Borthwick and Foote [33]. The UKCRF wave basin has a working area of 20 m longshore by 15 m cross-shore. Waves are produced using a 72-paddle wavemaker, and periodic lateral boundary conditions are provided by a 4-pump longshore current recirculation system. Three sinusoidal cusps were constructed on the upper section of a 1:20 plane beach whose toe was located 8 m from the wavemaker. The still water depth was 0.5 m at the wavemaker. In the cuspate region, the bed topography was given by

$$h_s(x,y) = s\left[(x_L - x) - A\sin\left(\frac{\pi(x_L - x)}{x_L}\right)\left(1 + \sin\left(\phi - \frac{2\pi y}{R}\right)\right)\right] \tag{32}$$

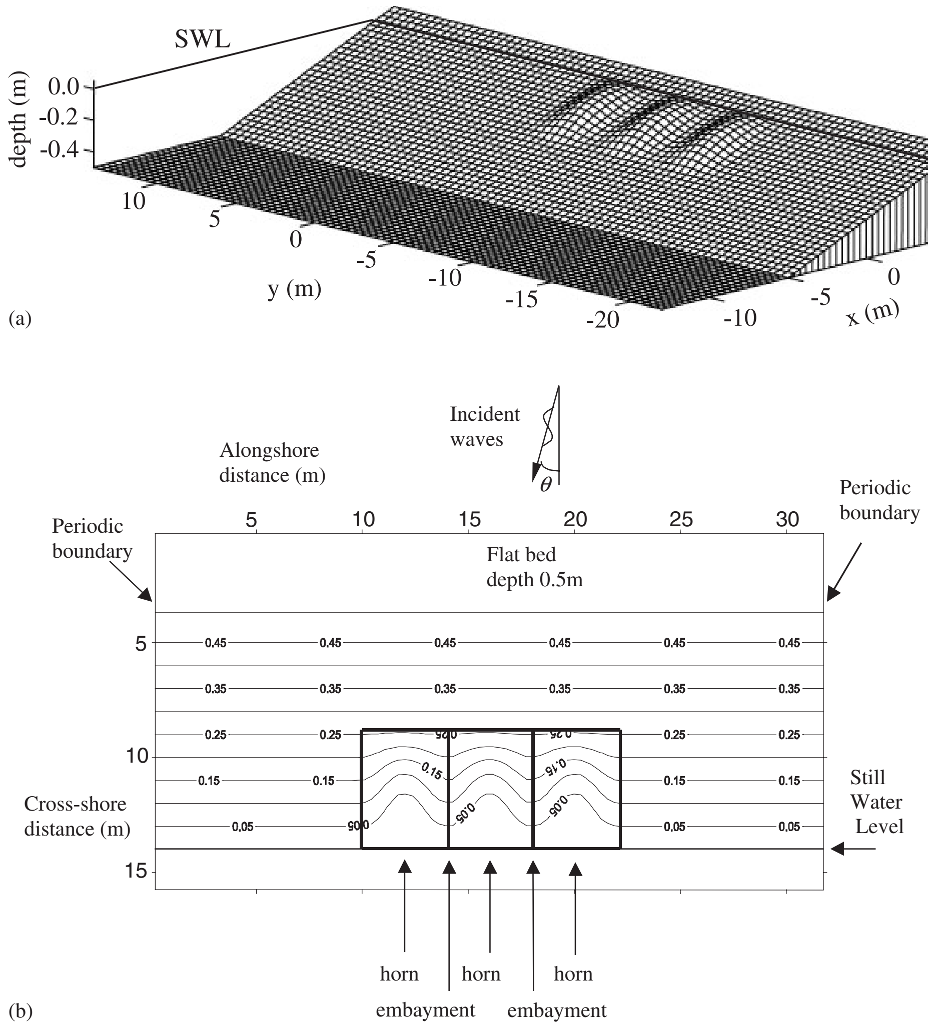

Figure 13. Tricuspate beach: (a) Location of cusped beach in the UKCRF; and (b) bed topography used in the numerical simulation.

where $s = 0.05$ is the bed slope, x is the distance onshore from the toe of the cusps, $x_L = 5\,\text{m}$ is the length of one cusp cross-shore, y is the distance alongshore from the start of the cusps, $A = 0.75$ is an amplitude related to cusp height, $R = 4\,\text{m}$ is the longshore wavelength of a cusp, and $\phi = 3\pi/2$ is a phase angle. Figure 13(a) presents a distorted scale 3-D view of the bed topography of the tri-cuspate beach in the UKCRF. Figure 13(b) illustrates the corresponding still water depth contours that delineate the beach used in the numerical model.

Borthwick and Foote [33] obtained estimates of the horizontal components of the wave-induced currents by tracking the movements of neutrally buoyant markers using digital image analysis. Acoustic Doppler velocimetry was used to determine the detailed 3-D velocity com-

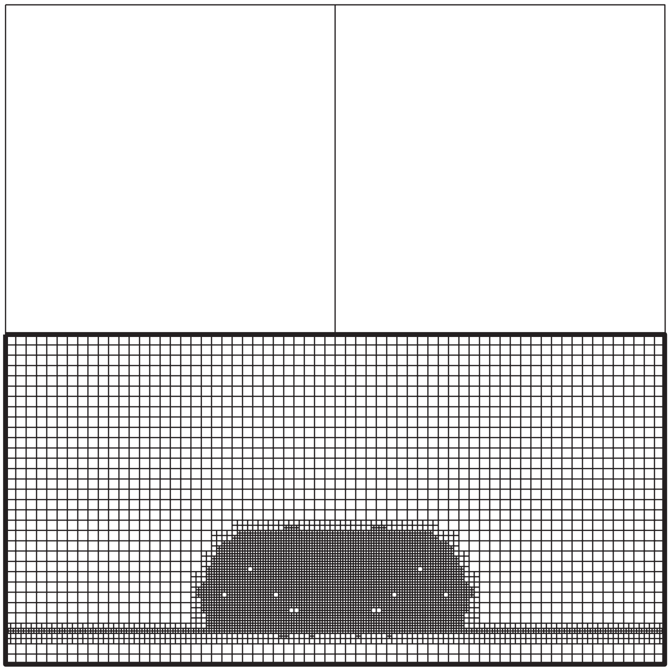

Figure 14. Adapted quadtree grid for case B.

ponent profiles through the depth at selected points in the nearshore zone. Of the four wave conditions investigated by Reference [33], two are used here for model verification; namely:

Case B (regular normally incident waves): $H_o = 0.125$ m, $T = 1.2$ s, $\theta_o = 0°$;

Case C (regular obliquely incident waves): $H_o = 0.125$ m, $T = 1.2$ s, $\theta_o = 20°$,

where H_o and θ_o are the offshore wave height and direction of the incident waves, respectively, and T is the wave period.

For both cases considered, the numerical model was first implemented on fixed uniform quadtree grids. Grid convergence was achieved using a level-8 grid of 128×256 cells where $\Delta x = \Delta y = 0.046875$ m. In all simulations, $\Delta t = 0.01$ s, and the offshore wave height was ramped up to its steady-state value over 20 s. $M_T = 1.0$, $R_h = 0.001$ m inside the cuspate region, and $R_h = 0.02$ m elsewhere. Periodic conditions were imposed at the lateral boundaries. Grid adaptation was invoked on a uniform level-6 base grid of 32×64 cells where $\Delta x = \Delta y = 0.1875$ m. Using Criterion II, mesh enrichment occurred if $V_s > 0.06$, and mesh depletion if $V_s < 0.048$. The mesh was adapted every 10 time steps, with minimum and maximum subdivision levels set to 6 and 8, respectively.

Figure 14 illustrates the converged adapted grid of 6386 cells corresponding to the steady state solution for the normally incident waves of case B. The corresponding level-8 uniform grid contains 32768 cells, of which most are effectively redundant, thus demonstrating the advantage of using dynamic grid adaptation to allocate computational resources in areas of high flow gradient. Figures 15(a), 15(c) show the predicted steady-state wave-induced current vectors and stream function contours. The filtered current patterns in Figure 15(c) are in

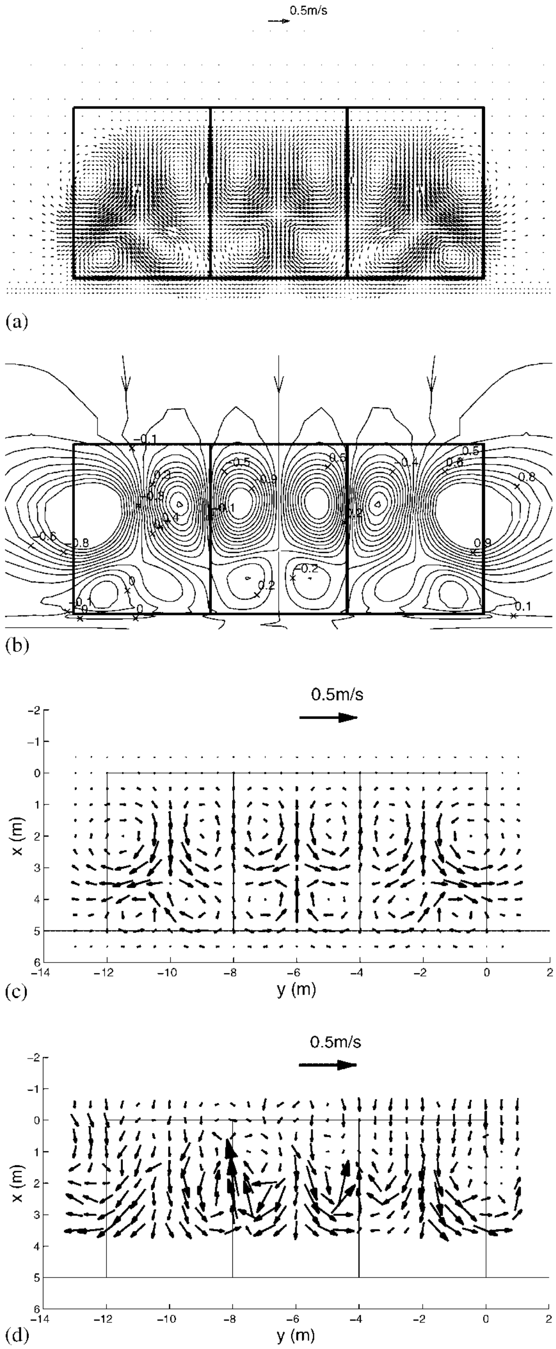

Figure 15. Numerical predictions and experimental measurements: Case B: (a) Numerical depth-averaged velocities; (b) numerical depth-averaged stream function contours; (c) filtered numerical depth-averaged velocities; and (d) experimental velocities.

reasonable agreement with the experimental data from Reference [33] in Figure 15(d), with primary circulation zones evident in the vicinity of the breaker zone. Narrow seaward-flowing rip currents are visible, and coincide with the narrowing of the streamlines in Figure 15(b). The magnitude of the predicted rip currents is lower than that obtained experimentally, presumably due to period-averaging and linearization of the governing equations smoothing out the jet-like motion of the measured rip currents [33, 34]. It should be noted that the measured data include inertia effects of the markers, as well as interpolation errors from projecting the current velocities onto a uniform grid. Also evident in the numerical results are secondary circulation patterns in the swash zone. In both cases B and C, these secondary gyres could not be quantified experimentally because the markers began to hit the bed in the shallowest water. However, the presence of secondary circulation cells was qualitatively confirmed by observing the movement of dye close to the shore.

Results for case C, where waves approach the beach obliquely, are shown in Figure 16. Here, a longshore current is generated at the plane beach, which then becomes a meandering longshore current following the bed contours in the tri-cuspate region. In general, there is close agreement between the numerical experimental current patterns and strengths, even at the limit of the experimental measurements in the shallowest water where secondary recirculation zones are discernible. The computed stream-function plot in Figure 16(b) shows that the secondary recirculation zones near the shoreline are weak.

Within the conceptual framework of the coupled ray-type wave conservation equations and modified SWEs, the nearshore currents can be readily explained in terms of the spatial gradients of radiation stresses (or local dissipation of the excess momentum flux due to waves) [19]. As the waves break, $\partial S_{xx}/\partial x$ reverses in sign and provides thrust to force the water up the beach, especially over the cusp horns. In the case of normally incident waves, the sinusoidally varying longshore gradients of S_{yy} give rise to a variation in the longshore-directed radiation stresses creating periodic longshore variations in the MWL and hence pressure gradients that drive currents toward each embayment. In turn, offshore-directed pressure gradients are generated sending rip currents beyond the surf zone. The major difference between the normally and obliquely incident cases is due to S_{xy} $(=S_{yx})$ and the associated spatial gradients. Unlike the case when $\theta_{\mathrm{o}}=0°$, the combined thrust of $\partial S_{yx}/\partial x$ and $\partial S_{yy}/\partial y$ for obliquely incident waves acts entirely in the negative y-direction and is the direct cause of the meandering longshore current.

6. PARAMETER STUDY FOR MULTICUSPED BEACH

A parameter study has been undertaken to provide insight into wave-induced currents at a cusped beach, while also assessing the performance of the numerical model. Hence, the following changes were made to determine their effect on the solution:

(i) variation of the incident wave angle between $\theta=0$ and 60°;
(ii) reduction in the height of one of the cusps;
(iii) variation of the offshore wave height;
(iv) replacement of the tri-cuspate beach by an infinitely repeating series of cusps;
(v) variation of the eddy viscosity parameter M_{T}.

To aid interpretation, maximum rip and longshore current values are recorded in Table II.

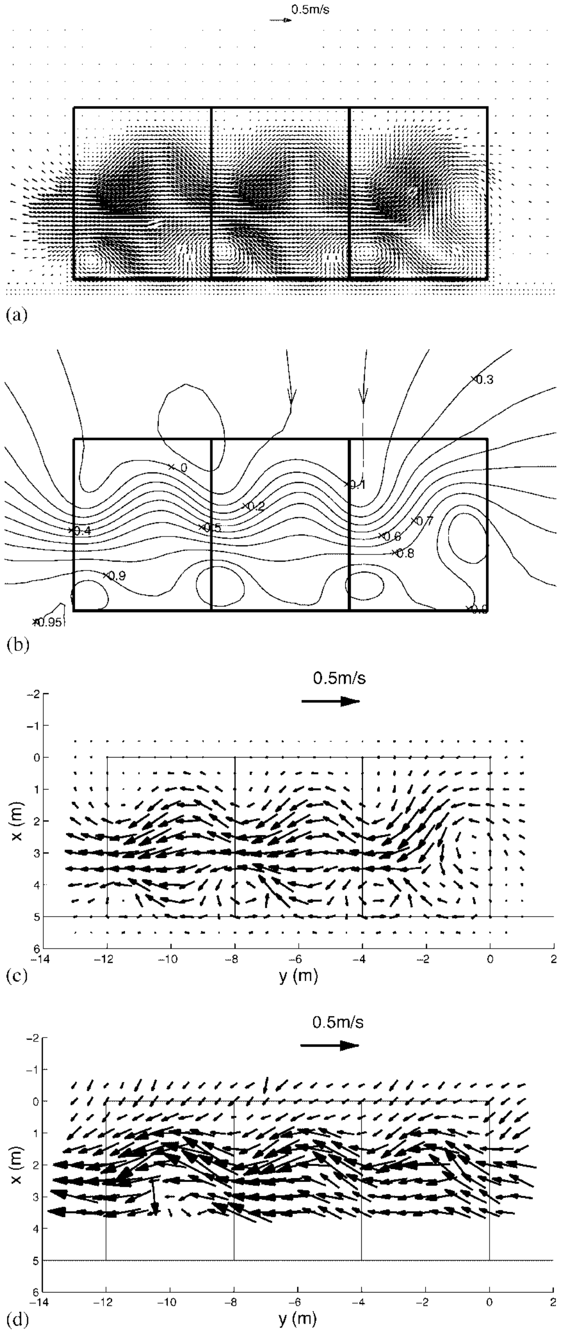

Figure 16. Numerical predictions and experimental measurements: Case C: (a) Numerical depth-averaged velocities; (b) numerical depth-averaged stream function contours; (c) filtered numerical depth-averaged velocities; and (d) experimental velocities.

Table II. Results for multicusp beach parameter tests.

Parameter change	Maximum rip current (m/s)	Maximum longshore current (m/s)	Number of cells[‡]
Case B, $\theta_o = 0°$[†]	−0.174	−0.217	6386
Case C, $\theta_o = 20°$[†]	—	−0.390	7625
Increase the incident wave angle to $\theta_o = 5°$	−0.161	−0.232	6353
Increase the incident wave angle to $\theta_o = 10°$	−0.134	−0.239	6272
Increase the incident wave angle to $\theta_o = 20°$	—	−0.390	7625
Reduce height of offcentre cusp by 5%	−0.155	−0.208	6308
Reduce height of offcentre cusp by 20%	−0.155	−0.208	6206
Reduce height of offcentre cusp by 40%	−0.154	−0.209	6092
Reduce height of offcentre cusp by 60%	−0.152	−0.209	5807
Infinite series of cusps, wave angle $\theta_o = 0°$	−0.174	−0.178	12128
Infinite series of cusps, wave angle $\theta_o = 20°$	—	−0.346	11960
Increase eddy viscosity parameter to $M_T = 1.10$	−0.145	−0.201	6290
Decrease eddy viscosity parameter to $M_T = 0.80$	−0.240	−0.253	6443
Decrease eddy viscosity parameter to $M_T = 0.25$	−0.257	−0.242	6881
Decrease eddy viscosity parameter to $M_T = 0.25$ with infinite series of cusps	−0.305	−0.249	13997

[†] Denotes original parameter values: $H_o = 0.125$ m, $R_h = 0.02$ m outside cusp region, $R_h = 0.001$ m inside cusp region, $M_T = 1.0$.

[‡] Reference grid number of cells for highest level uniform grid: 32768.

6.1. Variation of incident wave angle

Figure 17 presents the computed depth-averaged stream function contours at steady state for $\theta = 0$, 5, 10 and 20°. As θ increases, a meandering longshore current develops, but it is not until θ is about 10° that the longshore current is the dominant flow feature instead of the circulation zones. At $\theta = 5°$, the primary recirculation zones are strong (as displayed in the stream function plots), and there is a very weak longshore current from right to left. At $\theta = 10°$, the meandering longshore current is more evident, and the anticlockwise rotating primary and associated clockwise secondary circulation cells have disappeared. By $\theta = 20°$, transition to a full meandering longshore current is effectively complete. As the angle changes from 5 to 10°, the clockwise primary recirculation cells migrate leftwards as they are affected by momentum transfer from the growing meandering nearshore current. Between 10 and 20° these cells become progressively weaker and merge to form a large-scale re-circulating region offshore of the cusps. At larger incident wave angles ($\theta = 30, 45$ and $60°$), the meandering longshore current patterns do not change significantly and are not displayed.

These results demonstrate that the meandering longshore current arises from quite a small deviation from normal incidence. This is not surprising since even a small angle of incidence introduces gradients in the shear stress that can only be balanced by bottom friction, for which there needs to be a velocity.

6.2. Reduction in height of a cusp

Figure 18 illustrates the depth-averaged stream function contours with normally incident waves for cases where the cusp height has been reduced by 10, 20, 40 and 60%. The plots clearly

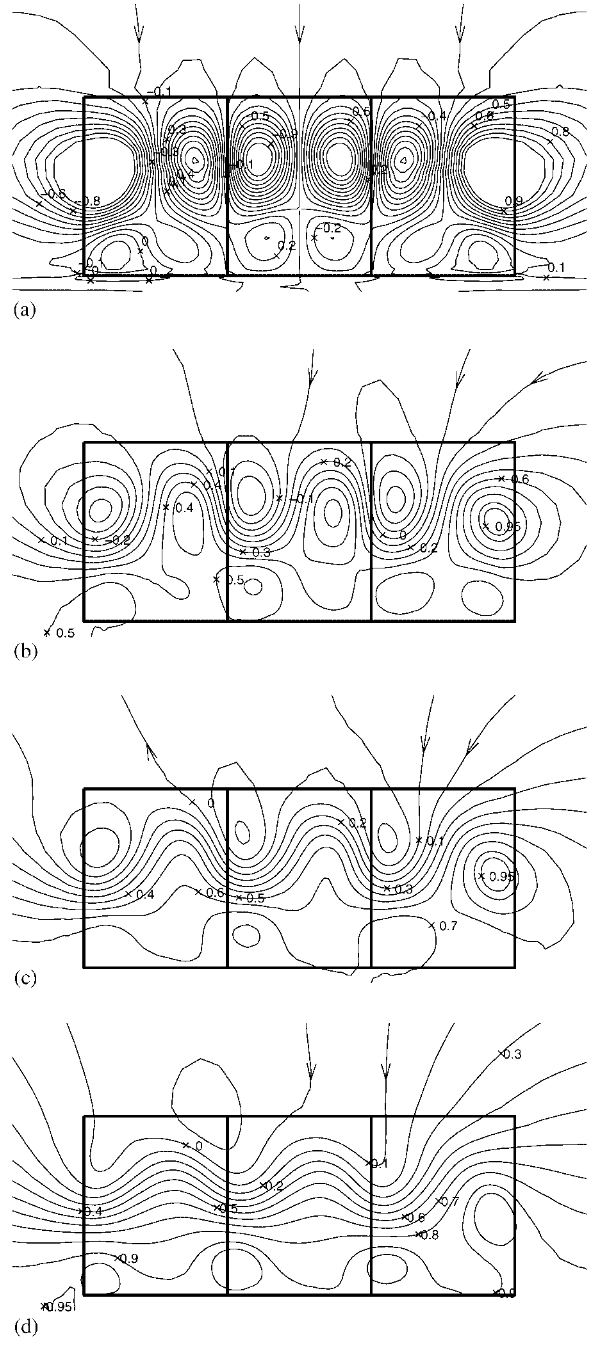

Figure 17. Predicted stream function contours: variation of incident wave angle: (a) $\theta = 0°$; (b) $\theta = 5°$; (c) $\theta = 10°$; and (d) $\theta = 20°$.

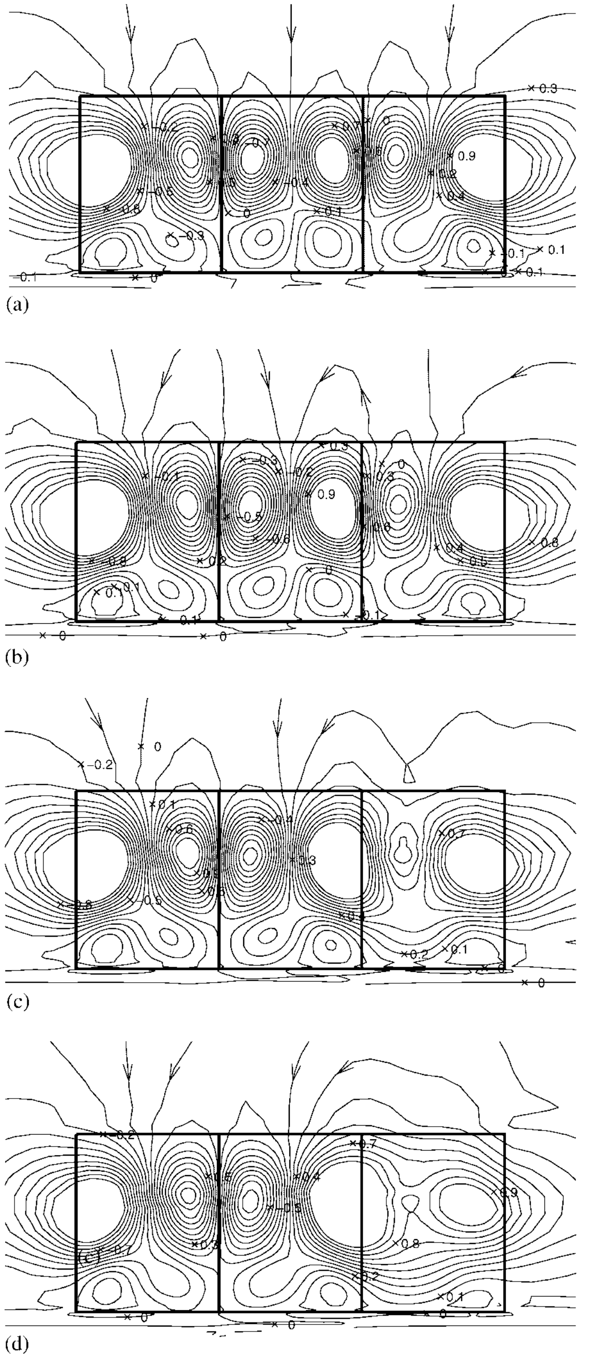

Figure 18. Predicted stream function contours: off-centre cusp height decrease: (a) 10% decrease; (b) 20% decrease; (c) 40% decrease; and (d) 60% decrease.

show that it is not until the cusp height is significantly reduced by 40% (Figure 18(c)), that the flow field in its vicinity is altered. Until this point, the strong circulating flows still occur indicating that the flow field is insensitive to relatively small changes in bed topography. When the cusp height is reduced to 60% (Figure 18(d)), it is obvious that the flow pattern at the central cusp becomes almost identical to that at the outer cusp before its height was reduced, as would be expected. At the reduced outer cusp, the originally strong gyres have virtually disappeared, while the secondary circulation zone immediately adjacent to the shoreline, has been replaced by a longshore feeder current. A reduction of the height of one cusp does not affect the maximum rip and longshore current speeds induced by the other cusps, Table II. The dependence of the circulation patterns on these topography changes also supports the idea that bathymetry- and wave-induced currents encourage the self-sustaining bedforms observed at cuspate shorelines [35].

6.3. Variation of the offshore wave height

The effect of offshore wave height on the nearshore current patterns is examined by setting H_o to values of 0.01, 0.05, 0.10 and 0.15 m. Figure 19 shows the depth-averaged velocities and streamlines for an offshore waveheight of $H_o = 0.01$ m. Although the velocities are very small, the streamlines in Figure 19(b) illustrate that the strongest circulation zones are generated near the breaker line with their centres approximately 1 m offshore of the still water line.

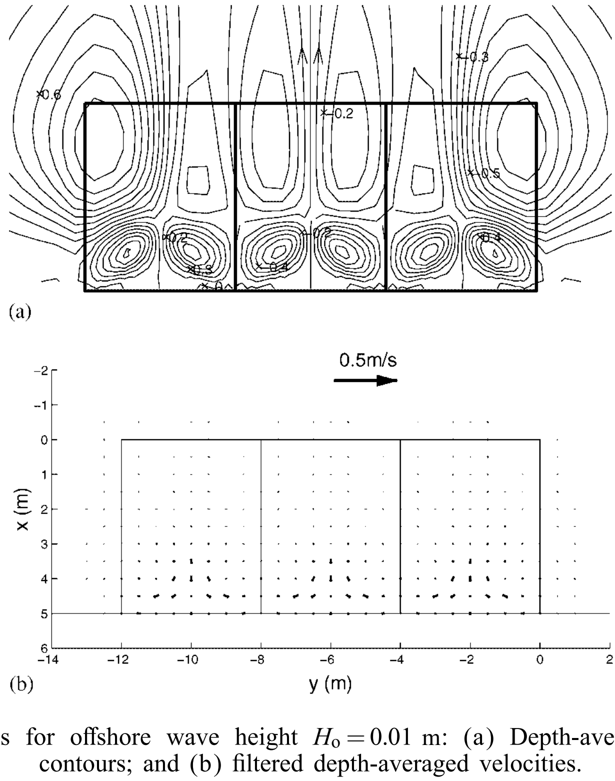

Figure 19. Predictions for offshore wave height $H_o = 0.01$ m: (a) Depth-averaged stream function contours; and (b) filtered depth-averaged velocities.

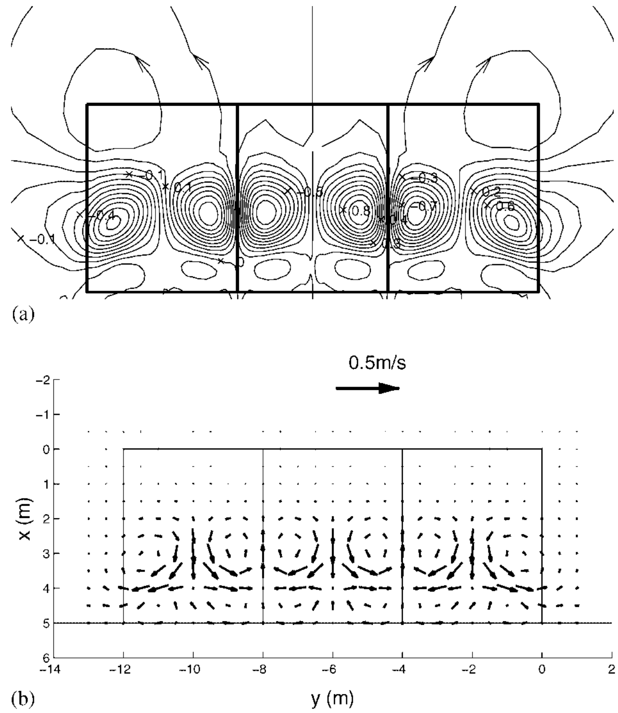

Figure 20. Predictions for offshore wave height $H_0 = 0.05$ m: (a) Depth-averaged stream function contours; and (b) filtered depth-averaged velocities.

These correspond to the primary circulation cells observed for Case B where $H_0 = 0.125$ m in Figure 15(b), but occur in shallow water near the shoreline without the well-defined secondary circulation cells observed previously. Although there is an offshore flow at the cusp troughs driven by the primary recirculation cells, the flow path is relatively broad and weak, unlike a rip-like jet. Offshore of the primary recirculation zones there are even weaker counter-rotating cells of opposite sense of rotation. This means that at the toe of the cusp horn, the flow is offshore directed when $H_0 = 0.01$ m, unlike the situation when $H_0 = 0.125$ m in Case B. If the offshore waveheight increases slightly to $H_0 = 0.05$ m, the circulation patterns alter. The primary circulation cells have streamlines closely spaced at embayments, linked to offshore-directed rip-like currents. It would appear that given an appropriate bathymetry, a relatively small offshore waveheight may be sufficient to trigger the formation of a rip current. The stream function contours in Figure 20(a) reveal that the primary recirculation cells have moved offshore, allowing the formation of weaker secondary circulations in the shallowest waters. However, comparison of the weak offshore circulation zones with those produced by $H_0 = 0.125$m of Case B shows the flow direction in this region is still opposite to that observed at larger wave heights. Figure 21 illustrates the streamlines when the offshore waveheight is increased to $H_0 = 0.10$ m. There is a pronounced shift in the flow pattern, which more closely resembles that obtained for Case B in Figure 15(b). The primary circulation cells have moved slightly further offshore and the secondary circulation cells have widened cross-shore relative

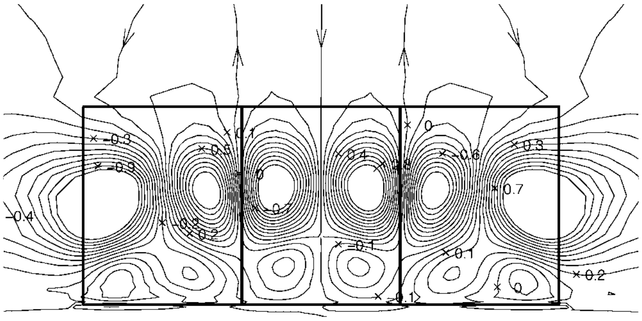

Figure 21. Predictions for offshore wave height $H_o = 0.10\,\text{m}$. Depth-averaged stream function contours.

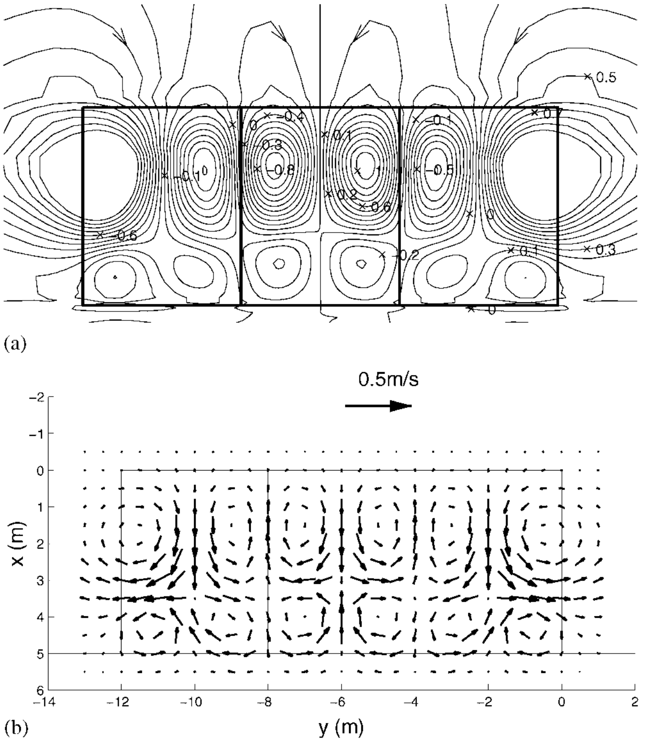

Figure 22. Predictions for offshore wave height $H_o = 0.15\,\text{m}$: (a) $H_o = 0.05\,\text{m}$: Depth-averaged stream function contours; and (b) filtered velocities.

to the case of $H_o = 0.05\,\text{m}$. The rip-like currents have narrowed and flow further from the beach before they fan out and die away outside the surf zone. If the offshore waveheight is increased further to $H_o = 0.15\,\text{m}$, as shown in Figure 22, there is only a marginal change in the wave-induced current patterns. This is due to the gradients of the radiation stresses inside the surf zone being limited in magnitude by saturated wave breaking. Overall, it appears that there is a shift in circulation patterns as cuspate bedforms develop, closely linked to feedback between the changing morphology and wave-induced currents.

6.4. Infinitely repeating series of beach cusps

Rhythmic shorelines often consist of multiple cusps, and so it is important to examine whether the findings from three cusps can be extended to multiple cusps, using periodic lateral boundary conditions. Here, the bed roughness remains $R_h = 0.001$ m in the cuspate region and 0.02 m elsewhere, in accordance with the UKCRF experiments. To compare with the tri-cuspate beach data for Cases B and C, waves of offshore wave height $H_0 = 0.125$ m of zero angle of incidence and 20° angle, respectively, are generated at the offshore boundary. The predicted depth-averaged streamline patterns in Figure 23(a) repeat exactly per cusp, and consist of identical strong primary nearshore gyres, weaker secondary circulation zones immediately adjacent to the shoreline and very weak circulation in the offshore region. For the 20° case, a steady meandering longshore current and weak secondary circulation zones adjacent to the shoreline are obtained as illustrated in Figure 23(b). These computational patterns suggest that the experimental flow features observed around the central cusp of the tri-cuspate beach are representative of those at a beach with repeating cusps.

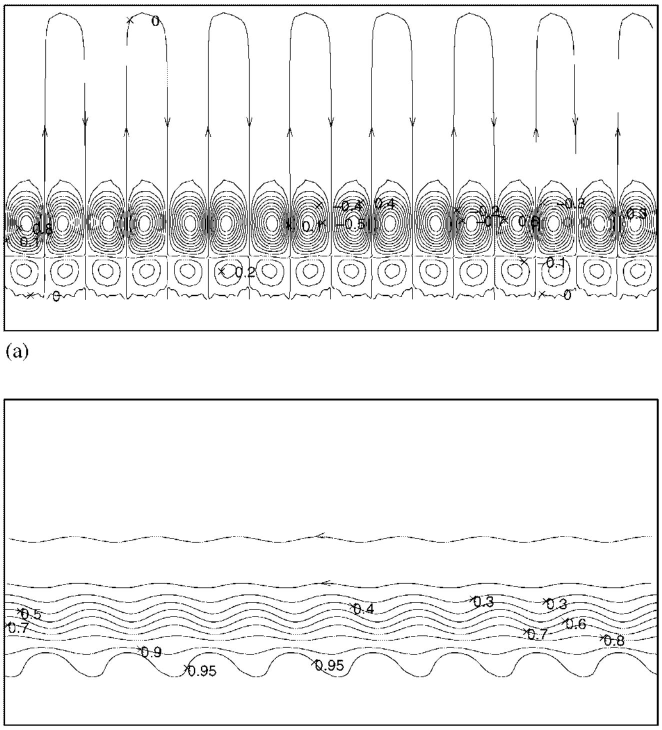

(a)

(b)

Figure 23. Predicted stream function contours: variation of wave angle over repeating cusps: (a) $\theta = 0°$; and (b) $\theta = 20°$.

6.5. Variation of the dimensionless eddy viscosity parameter M_T

In the numerical scheme, the eddy viscosity model of Reference [22], Equation (13), accounts empirically for lateral mixing of horizontal momentum. O'Connor and Yoo [36] showed that Thornton's model performs satisfactorily when simulating a longshore current due to oblique waves at a beach. However, Haller and Dalrymple [34] found that the turbulent mixing terms have a significant influence on the nature of predicted nearshore rip-like currents. Here, Thornton's empirical parameter, M_T, has been varied to assess the effect of changing eddy viscosity levels on the nearshore currents due to waves at normal incidence. An increase in M_T to 1.1 caused slight reductions in the maximum rip and longshore currents (see Table II).

When decreasing M_T, the first noticeable effects on the flow patterns occur at $M_T = 0.5$ approximately. The size and orientation of the primary circulation zones change; there is a broader area of onshore flow, and stronger rip currents cut diagonally across the surf zone. Figure 24(a) depicts the depth-averaged stream function contours when M_T has been further decreased to 0.25. Detailed comparison with the results for Case B in Figure 15(b) where $M_T = 1.0$ reveals that decreasing M_T has exaggerated the very slight orientation of the original central circulation zones. Thus, the rip currents that are meant to be the fastest part of the flow experience the maximum effect of changes in the eddy viscosity.

Given the spreading of the circulation zones over adjacent cusps at the tri-cuspate beach, it is of interest to see if similar behaviour is exhibited over the infinitely repeating series of cusps described previously. Figure 24(b) illustrates the depth-averaged stream function contours at the multi-cusped beach when $M_T = 0.25$. In contrast to the results for the tri-cuspate beach in Figure 24(a), the recirculation zones are once more oriented normal to the shore. Furthermore, the repeated primary circulation cells are elongated cross-shore; the onshore flow at the cusp horns covers a wider area, and the seaward currents are narrower and stronger. Clearly, at a beach with successively repeating cuspate bedforms, there is a balance of longshore momentum in the flow field between adjacent cusp horns that does not exist at a tri-cuspate beach. Moreover, if the nearshore flow-induced turbulence falls below a certain level, the flow field in the centre of a tri-cuspate beach may not be representative of a beach with repeating cuspate bedforms.

7. CONCLUSIONS

A finite-volume numerical model has been presented for coastal wave–current interaction at cuspate beaches, based on adaptive hierarchical grids. The governing depth- and period-averaged (2-DH) equations are formulated as a set of hyperbolic conservation laws to permit flows to be modelled with Roe's approximate Riemann solver to solve flux terms. A matrix hyperbolic formulation of the wave energy and kinematic wave number conservation laws is derived, and its eigensystem determined. The eigenvalues are equal to the wave group celerity (corresponding to the rate of transport of energy) and modified wave group celerities (corresponding to wave front components) as they propagate into shallower water.

Various quadtree grid adaptation criteria have been investigated for simulating nearshore circulation at a half-sinusoidal beach. Significant gains have been achieved in memory storage and computational time by using grid adaptation. Of the various adaptation criteria examined, those based on non-dimensionalized depth-averaged vorticity, wave-height gradient,

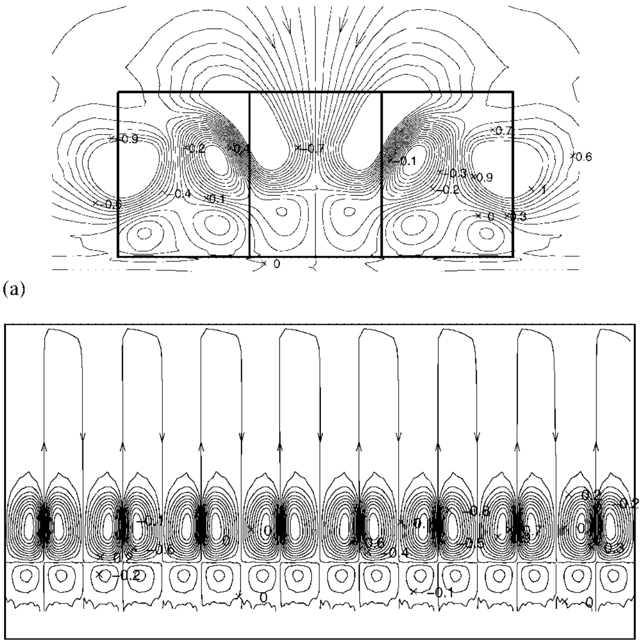

(a)

(b)

Figure 24. Predicted stream function contours: eddy viscosity parameter $M_T = 0.25$: (a) Tricuspate beach (cuspate area enlarged); and (b) repeating cusps (entire numerical domain).

wave steepness and the magnitude of velocity gradients produced grids that were locally refined around the corresponding physical features with a sensible distribution of cells. The wave steepness criterion provides mesh enrichment around the wave-breaking zone, whereas the magnitude of velocity gradients criterion focuses on flow regions with large spatial gradients in the wave-induced currents. An attempt to remove automatic dependence on cell size using a criterion based on non-dimensionalized wave-height gradient produced unstable results. We conclude that physical criteria lead to more accurate and stable results than mixed physical and grid criteria, where feedback tends to occur between the grid and the physical flow features.

The simultaneous combination of different adaptation criteria produced spurious results due to interference between cell addition and removal according to the separate criteria. However, when all the criteria are satisfied simultaneously, combining the criteria eliminates negative feedback and the simulation remains stable. An investigation into the efficiency gains attained by implementing adaptation after different numbers of time steps, showed that occasional adaptation leads to a marginal decrease in cpu-time over adaptation each time step.

The numerical model has been further tested by simulating wave–current interaction at a tri-cuspate beach, and the results are found to be in reasonable agreement with laboratory data from the UKCRF from Borthwick and Foote [33]. Additional insight into the nearshore processes at cusped beaches has been gained from a parameter study, which examined the sensitivity of the horizontal wave-induced currents to the angle of wave incidence, relative cusp height, offshore wave height, repeating cuspate bedforms and turbulent eddy viscosity. The results indicate that the circulation zones are highly localized to within the smooth cuspate region, and that a meandering longshore current can be initiated by a small deviation from the normal by the incident wave angle.

The work described herein has concentrated on idealized 2-DH nearshore wave-induced currents at fixed multi-cusped beaches. Of course, two-dimensional period-averaged ray-type modelling is inherently limited. Wave reflection is not modelled, due to the loss of phase information. Vertical motions are neglected, and so the undertow is not predicted. Energy dissipation mechanisms such as wave breaking and turbulence are treated empirically. Despite these limitations, our relatively simple 2-DH model apparently reproduces much of the dominant physics in such a complex coastal flow. To predict coastal processes at sandy beaches, an obvious extension of our work is to incorporate sediment dynamics and morphological response.

Overall, this paper demonstrates some of the computational advantages of a Godunov finite-volume approach on an adaptive quadtree mesh. In such a framework, mesh adaptation based on a single criterion is simple and effective in generating accurate representations of localized complex physical features of coastal flows.

ACKNOWLEDGEMENTS

This work has been supported by the U.K. Engineering and Physical Sciences Research Council through EPSRC Grant GR/L29877, and co-investigated by Dr K. Anastasiou and Dr Zacharenia Skoula of Imperial College, London.

REFERENCES

1. Birkby P, Cant RS, Savill AM. Application of a laminar flamelet model to confined explosion hazards. *Flow, Turbulence and Combustion* 2000; **63**(1):361–377.
2. De Zeeuw D, Powell KG. An adaptively refined Cartesian mesh solver for the Euler equations. *Journal of Computational Physics* 1993; **104**:56–68.
3. Thompson JF, Soni BK, Weatherhill NP. *Handbook of Grid Generation*. CRC Press LLC: Boca Raton, 1999.
4. Zienkiewicz OC, Zhu JZ. A simple error estimator and adaptive procedure for practical engineering analysis. *International Journal for Numerical Methods in Engineering* 1987; **24**:337–357.
5. Sleigh PA, Gaskell PH, Berzins M, Wright NG. Unstructured finite-volume algorithm for predicting flow in rivers and estuaries. *Computers and Fluids* 1998; **27**(4):479–508.
6. Wu DH, Currie IG. Analysis of á-posteriori error indicator in viscous flows. *International Journal for Numerical Methods for Heat and Fluid Flow* 2002; **12**(3):306–327.
7. George PL. *Automatic Mesh Generation*: *Application to Finite Element Methods*. Wiley: New York, 1991.
8. Ivanenko SA, Muratova GV. Adaptive grid shallow water modelling. *Applied Numerical Mathematics* 2000; **32**(4):447–482.
9. Borthwick AGL, Cruz Léon S, Józsa J. The shallow water equations solved on adaptive quadtree grids. *International Journal for Numerical Methods in Fluids* 2001; **37**:691–719.
10. Rogers B, Fujihara M, Borthwick AGL. Adaptive Q-tree Godunov-type scheme for shallow water equations. *International Journal for Numerical Methods in Fluids* 2001; **35**:247–280.
11. Borthwick AGL, Park K-Y. Quadtree grid numerical model of nearshore wave-current interaction. *Coastal Engineering* 2001; **42**:219–239.
12. Hubbard M, Dodd N. A 2D numerical model of wave run-up and overtopping. *Coastal Engineering* 2002; **47**:1–26.
13. Hubbard M, Garcia-Navarro P. Flux difference splitting and the balancing of source terms and flux gradients. *Journal of Computational Physics* 2000; **165**:89–125.
14. Toro EF. *Shock-Capturing Methods for Free-Surface Flows*. Wiley Ltd: UK, 2001.
15. Dean RG, Dalrymple RA. *Water Wave Mechanics for Engineers and Scientists*. Prentice-Hall Inc: NJ, 1984.
16. Yoo D. Mathematical Modelling of Wave–Current Interacted Flow in Shallow Waters. *Ph.D. Thesis*, University of Manchester, UK, 1986.

17. Battjes JA. Refraction of water waves. *Journal of Waterway*, *Port*, *Coastal and Ocean Engineering* 1968; **94**(WW4):437–451.
18. Yoo D, O'Connor BA. Diffraction of waves in caustics. *Journal of Waterway*, *Port*, *Coastal and Ocean Engineering* 1988; **114**(6):715–731.
19. Longuet-Higgins MS, Stewart RW. Radiation stress and mass transport in gravity waves with application to 'surf beat'. *Journal of Fluid Mechanics* 1962; **13**:481–504.
20. Bijker EW. The increase of bed shear in a current due to wave motion. *Proceedings of the 10th International Conference on Coastal Engineeringg* (ASCE) 1966; 746–765.
21. US-CERC. *Shore Protection Manual*. U.S. Army Coastal Engineering Research Center, U.S. Corps of Engineers, Washington, DC, 1984.
22. Thornton EB. Variation of longshore current across the surf zone. *Proceedings of the 12th Conference on Coastal Engineering* (ASCE) 1970; 291–308.
23. Svendsen I, Putrevu U. Surf-zone hydrodynamics. In *Advances in Coastal and Ocean Engineering*, PL-F Liu (ed.), vol. 2. World Scientific: Singapore, 1996; 1–77.
24. Roe PL. Approximate Riemann solvers, parameter vectors, and difference schemes. *Journal of Computational Physics* 1981; **43**:357–372.
25. Rogers B, Borthwick AGL, Taylor PH. Balancing flux gradients and source terms with Roe's approximate Riemann solver. *Journal of Computational Physics* 2003; **192**(2):422–451.
26. Hirsch H. *Numerical Computation of Internal and External Flows*, vol. 2. Computational methods for inviscid and viscous flows. John Wiley & Sons: New York, 1990.
27. Harten A, Hyman JM. Self adjusting grid methods for one-dimensional hyperbolic conservation laws. *Journal of Computational Physics* 1983; **50**:235–269.
28. Ebersole BA, Dalrymple RA. Numerical modeling of nearshore circulation. *Proceedings of the 10th International Conference on Coastal Engineering* (ASCE) 1980; **4**:2710–2725.
29. Greaves DM, Borthwick AGL. Hierarchical tree-based finite element mesh generation. *International Journal for Numerical Methods in Engineering* 1999; **45**:447–471.
30. Greaves DM, Borthwick AGL. On the use of adaptive hierarchical meshes for numerical simulation of separated flows. *International Journal for Numerical Methods in Fluids* 1998; **26**:303–322.
31. da Silva Lima S. Wave-induced nearshore currents. *Ph.D. Thesis*, Liverpool University, U.K., 1981.
32. Roache PJ. Perspective: a method for uniform reporting of grid refinement studies. *Journal of Fluids Engineering* 1994: **116**:405–413.
33. Borthwick AGL, Foote YLM. Wave-induced nearshore currents at a tri-cuspate beach in the UKCRF. *Proceedings of Institute of Civil Engineers* 2002; **4**:251–263.
34. Haller MC, Dalrymple RA. Rip Current Instabilities. *Journal of Fluid Mechanics* 2001; **433**:161–192.
35. Komar PD. *Beach Processes and Sedimentation* (2nd edn). Prentice-Hall: NJ, USA, 1998.
36. O'Connor B, Yoo D. Turbulence modelling of surf zone mixing processes. *Proceedings Specialty Conference On Coastal Hydrodynamics* (ASCE) 1987; 371–383.

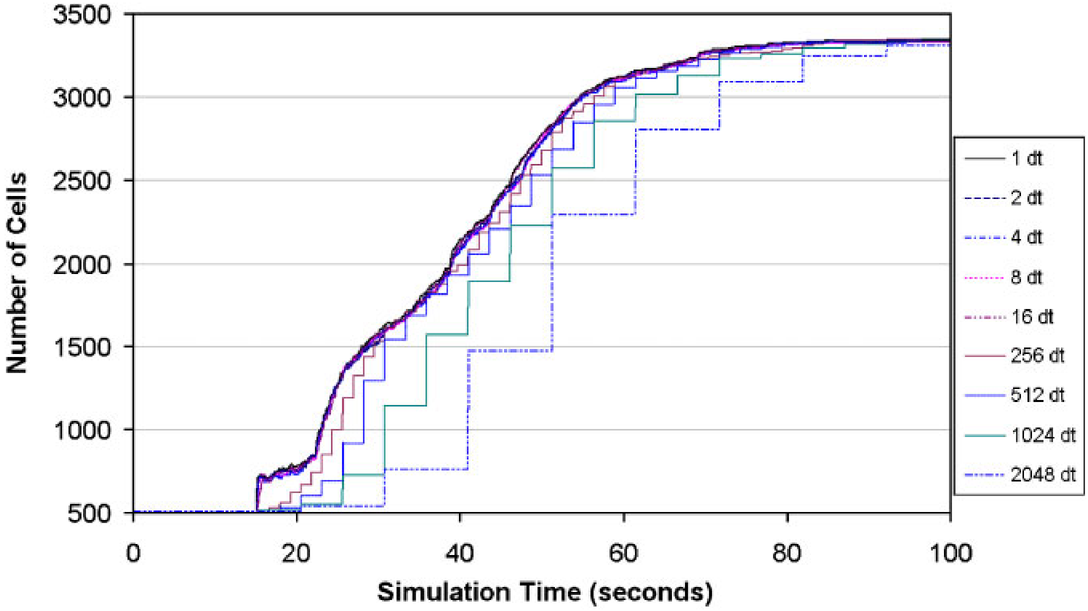

Plate 1. Number of cells with simulation time using adaptation criterion based on velocity gradient magnitude.